ELSEVIER

Contents lists available at ScienceDirect

# Science of Remote Sensing

journal homepage: www.journals.elsevier.com/science-of-remote-sensing



Full Length Article

Surface heights and crevasse morphologies of surging and fast-moving glaciers from ICESat-2 laser altimeter data - Application of the density-dimension algorithm (DDA-ice) and evaluation using airborne altimeter and Planet SkySat data



Ute C. Herzfeld a,\*, Thomas Trantow a, Matthew Lawson a, Jacob Hans a, Gavin Medley b

- <sup>a</sup> Geomathematics, Remote Sensing and Cryospheric Sciences Laboratory, Department of Electrical, Computer and Energy Engineering, University of Colorado Boulder, Colorado, 80309-0574, USA
- b Laboratory for Atmospheric and Space Physics, University of Colorado Boulder, Boulder, CO, USA

#### ARTICLE INFO

Keywords:
Laser altimetry
Density-dimension algorithm
ICESat-2
Glaciology
Glacier surging
Planet SkySat imagery

## ABSTRACT

NASA's Ice, Cloud and land Elevation Satellite ICESat-2, launched September 15, 2018, carries the first spaceborne multi-beam micro-pulse photon-counting laser altimeter system, the Advanced Topographic Laser Altimeter System (ATLAS). Observations from ATLAS are acquired in three pairs of weak and strong beams with 0.7 m nominal along-track spacing (under clear-sky conditions). The recording of the observations as a photon point cloud, which includes signal and background/noise events, requires a dedicated algorithm for identification of signal photons and determination of surface heights. The objectives of this paper are to demonstrate that measurements from ICESat-2 allow determination of heights over heavily crevassed ice surfaces and yield elevation profiles that present morphological characteristics that are typical of fast-moving and accelerating glaciers. Surface-height determination from the photon point cloud is facilitated by the density-dimension algorithm for ice surfaces, the DDA-ice. The DDA-ice returns surface heights at the 0.7 m sensor resolution for strong and weak beams, it utilizes a radial basis function for data aggregation and automatically adapts to changing environmental conditions and background characteristics, including time of day and apparent surface reflectance. In contrast, the official Land-Ice Along-Track Height Product, ATL06, provides surface heights at 40 m resolution with 20 m postings. The DDA-ice signal classification consistently identifies photons from complex reflectors in both the strong and weak ATLAS beams and hence constitutes a significant advance over the signal classification on the ATLO3 Global Geolocated Photons Product. Results are evaluated using (1) airborne laser altimeter data collected during our ICESat-2 validation campaign over Negribreen, Svalbard, during surge, and (2) high-resolution (0.72 m or 0.86 m) satellite image data from Planet SkySat acquired over Ilulissat Ice Stream (Jakobshavn Isbræ), Greenland. Using DDA-ice analysis, ICESat-2 data allow discrimination of ice-surface types from surging glaciers (Negribreen) and continuously fast-moving and accelerating glaciers (Jakobshavn Isbræ) based on morphological characteristics.

## 1. Introduction

On September 15, 2018 NASA launched the Ice, Cloud and land Elevation Satellite ICESat-2 to collect laser altimeter data aimed at deriving surface heights of the marine and terrestrial cryosphere, and to observe heights of other Earth surfaces, including land, inland water, ocean, as well as atmospheric layers. A main objective of the mission is to provide height information that will allow to understand changes in the

cryosphere that occur in the present realm of a changing climate.

A multi-beam micro-pulse photon-counting laser altimeter was selected as the instrument for the ICESat-2 mission, because the resultant data can be expected to capture the spatial and temporal variability in ice-surface height that is required to understand those processes that drive rapid changes in the cryosphere (Abdalati et al., 2010; Markus et al., 2017), foremost melt events and glacial acceleration. Glacial acceleration is the largest source of uncertainty in assessment of sea-level

E-mail address: Ute.Herzfeld@colorado.edu (U.C. Herzfeld).

<sup>\*</sup> Corresponding author.

rise (SLR) in the current realm of climatic warming, according to the Fifth Assessment Report (AR 5) of the Intergovernmental Panel on Climate Change (IPCC) (Stocker et al., 2013). In 2012, unprecedented large melt events that affected much of the Greenland Ice Sheet drove home the notion that the Greenland Ice Sheet has already entered a different realm regarding surface mass balance (SMB) (Nghiem et al., 2012; Hall et al., 2013; Tedesco et al., 2013).

Glacial acceleration is typically accompanied by surface elevation change and mass transfer. Especially for outlet glaciers of the Greenland and Antarctic ice sheets, acceleration leads to increase in SLR (Herzfeld et al., 2012; Bindschadler et al., 2013; Nowicki et al., 2013a, 2013b). The most conspicuous effect of rapid acceleration is the occurrence of heavy crevassing. Crevassing constitutes both a challenge and an opportunity to investigate change processes in glaciers (Herzfeld and Mayer, 1997; Van der Veen, 1998; Herzfeld et al., 2004). We have shown that distribution, shape and patterns of crevasses can be employed to derive information on ice dynamics, using spatial surface roughness and deformation as mathematical and physical vehicles in analysis of observations and numerical modeling (Mayer and Herzfeld, 2000; Trantow and Herzfeld, 2018). The first objective of this paper is to show that such information can be retrieved from ICESat-2 data.

Crevassing and other types of complex ice-surface morphology have been known to complicate retrieval of surface height using (pulselimited) radar and laser altimetry. Features at a scale smaller than the sensor's resolution have been summarized as sub-scale roughness, understood as generally broadening the signal (Davis, 1992; Davis and Marshak, 2004; Marshak and Davis, 2005; Miller and Hayne, 1972), but not as geophysical information of its own value. The objectives of this paper are to demonstrate that using ICESat-2 laser altimeter data, surface height in presence of complex ice surface morphology such as crevassing can (1) be measured and (2) employed to distinguish and characterize glaciers of different acceleration types. To address the second objective, we will contrast surface signatures of a currently surging Arctic glacier (Negribreen, Svalbard, located at (78.585°N, 18.809 E)) and the continuously fast-moving and accelerating Ilulissat Ice Stream (Jakobshavn Isbræ), Greenland, located at (69.096 N, 49.373 W). Comparing morphological details derived from ICESat-2 surface height profiles to high-resolution satellite imagery from SkySat (Planet), we will frame the potential for new levels of linking spatial characteristics to ice dynamics, both across the two acceleration types and for dynamic subregions within each dynamic prototype glacier.

The Advanced Topographic Laser Altimeter System (ATLAS), the main instrument aboard ICESat-2, is the first space-borne micropulse photon-counting multibeam (six-beam) lidar altimeter (Markus et al., 2017). Operating at 532 nm wavelength, ATLAS is designed to resolve ice-surface height at 0.7 m spacing along-track (under clear-sky conditions), using three pairs of a strong beam and a weak beam each. ATLAS records returns from every photon in the 532 nm wavelength of the sensor, which results in a photon point cloud (Neumann et al., 2019a). As a means to fully use the measurement capabilities of the micro-pulse photon-counting technology, we have developed a density-dimension algorithm for ice-surface analysis, the DDA-ice, which allows to accurately retrieve ICESat-2 surface heights even in regions of heavy crevassing or firn cover and under intermittent clouds (Herzfeld et al., 2017). The DDA-ice is an auto-adaptive algorithm that automatically adjusts its performance to environmental conditions and signal-noise relationships, such as those typical of day-time and night-time conditions and changes in apparent surface reflectance (ASR). Surface heights resultant from the DDA-ice have the resolution of the geolocated photon-data (0.7 m along-track postings under clear atmospheric conditions), interpolated by a ground follower that automatically adapts to surface roughness. We will show that the DDA-ice works for data from both the weak and the strong beams and for crevassed or complex as well as simple or smooth surface types. Algorithm results will be evaluated using two independently collected data sets: (1) Laser altimeter data from our ICESat-2 2019 validation campaign over Negribreen, Svalbard, and

(2) high-resolution (0.72 m or 0.86 m) satellite image data from Planet SkySat specifically acquired over Ilulissat Ice Stream (Jakobshavn Isbræ), Greenland.

In comparison, the standard land-ice along-track height product of ICESat-2, ATL06 (Smith et al., 2019a), is based on an algorithm suitable for analysis of large-scale elevation change of large regions such as the entire Greenland and Antarctic ice sheets (Smith et al., 2019b) and stands in the tradition of such large-scale analyses (Zwally et al., 2005; Wingham et al., 2006; Shepherd, 2012; Shepherd et al., 2018). With a 40-m along-track resolution with 20-m posting, the ATL06 product does not yield information on crevassed surfaces or other high-resolution morphological features and often fails to determine surface heights over such surface types.

The DDA-ice provides an alternative that facilitates inclusion of high-resolution surface signatures in investigations of cryospheric change processes, while also providing surface heights for undisturbed surfaces and a basis for regional and ice-sheet-wide assessment of surface elevation change and mass change. The high-resolution capability of the DDA-ice enables us to study glaciological events, such as rapid accelerations, and discriminate acceleration types. This will be demonstrated comparing height profiles from a currently surging glacier in the Arctic (Negribreen) and from the constantly fast-moving and accelerating Jakobshavn Isbræ (Figs. 1 and 2).

# 2. ICESat-2 mission, ATLAS measurement principles and derivation of the geolocated photon point cloud data (ATLO3)

#### 2.1. Overview

The ICESat-2 Mission concept and the main sensor, the ATLAS instrument, are described in (Markus et al., 2017) and (Neumann et al., 2019a). The resultant data that are used in this paper as input for the DDA-ice (ATLAS data product ATL03) are described in (Neumann et al., 2019a) and in the Algorithm Theoretical Base Document (ATBD) for the global geolocated photon data product, ATL03 (Neumann et al., 2019b).

ATLAS is a micropulse photon-counting multibeam (six-beam) lidar altimeter operating at 532 nm wavelength. It records signals from every single photon in the 532 nm domain of the sensor, including photon events that are returned signals from the sensor as well as photon events from background and instrument dark counts. This results in a point cloud of discrete photon returns and identification of the source of each photon event requires a specific algorithm. Especially during day-time operation, the majority of registered photon events stems from returns from ambient light. Hence the problem of identification of those photons that originate from the active sensor is an ill-posed mathematical problem, especially over complex terrain. The DDA-ice is an algorithm that solves this problem.

The DDA-ice is based on the geolocated photon cloud, as reported in the ATL03 product (and not on the signal classification provided in ATL03). The following subsections summarize information necessary to understand the measurement principles of ATLAS, the geometry of the data on the ground and essential steps leading to determination of the geolocated photon point cloud. Each photon is geolocated through application of geodetic corrections described in (Neumann et al., 2019a). Detailed algorithm descriptions are found in the ATBDs for the ATLAS product ATL02 (Level 1B) Data Product Processing (Martino et al., 2019), for ATL03g ICESat-2 Receive Photon Geolocation (Luthcke et al., 2019). Geophysical corrections are described in the ATBD for ATLAS data product ATL03 (Neumann et al., 2019b). The next subsections largely follow these references, with updated information added and observation geometries summarized in Fig. 3.

## 2.2. Transmitter, receiver, telemetering and cloud attenuation

ATLAS operates at 532 nm wavelength with pulse-repetition rate (PRF) of 10 kHz (exactly 532.272  $\pm$  0.15 nm). The PRF results in a

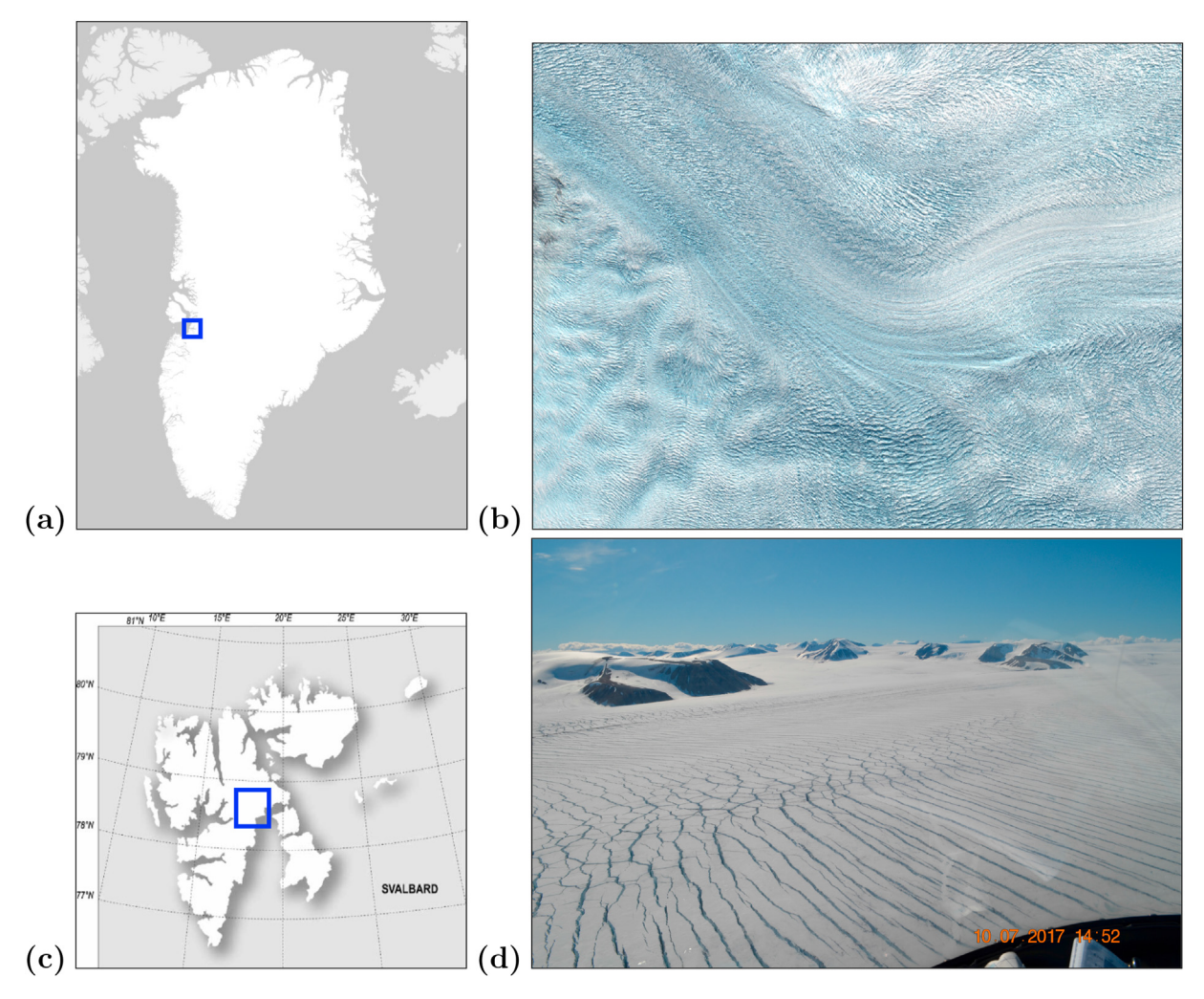


Fig. 1. Different crevasse types typical of (1) continued fast, accelerating movement (Jakobshavn Isbræ (Ilulissat Ice Stream), Greenland) and (2) surging (Negribreen, Svalbard) that may allow to discriminate acceleration types automatically in satellite altimetry. (a) Location map for Jakobshavn Isbræ, Greenland. (b) Jakobshavn Isbræ. Sentinel-2 RGB image acquired 2017-Apr-30, showing typical crevasses resultant from continued fast movement of the central ice stream, with fields of shear crevasses to the north and south of the central ice stream. (c) Location map for Negribreen, Svalbard. (d) Negribreen. Aerial image of typical clear-cut, recently opened surge crevasses, acquired 2017-Jul-10.

nominal 0.7 m spacing of laser pulses on the Earth's surface, under clear-sky conditions. The footprint diameter is less than 17.4 m, or less than 35 microradians ( $\mu$ rad) at 85% encircled energy. The pulse width is capped by 1.5 ns FWHM (full-width at half maximum). Pulse energy is 0.2–1.2 mJ, and beam energy is 175  $\pm$  17 mJ for a strong beam and 45  $\pm$  4 mJ for a weak beam, where nominal ratio of energy is 4:1 for strong:weak. The lasers are designed and built by Fibertek, Inc., using a master oscillator/power amplifier (MOPA) transmitter. It uses a Nd:YVO<sub>4</sub> gain crystal to generate infrared (1064 nm) light of the correct pulse width, which is frequency-doubled to generate the green 532 nm laser light for transmit. The single output beam is passed through a Diffractive Optical Element (DOE) to split it into 6 transmitted beams.

For redundancy, ATLAS carries two such lasers, only one is active at any given time. So far (at time of writing, January 2020), the first laser has been used, at energy level 4 of 10. The level was adjusted down from level 6 after an initial data collection phase, prior to science data collection.

The receiver is a telescope of 0.8 m diameter, with a Field of View (FOV) of 83.3  $\mu$ rad, resulting in a 45 m FOV on the Earth's surface. The maturity of a photon-counting detector technology was the deciding factor for use of green light (over 1064 nm near-infrared (NIR) light) (Neumann et al., 2019a). Nominal life time of the mission is 3 years, in which time about one trillion pulses will be fired.

The 532 nm signal is easily attenuated by clouds of moderate optical thickness. Atmospheric data are collected for a 14 km altitude range, recorded as shot sums for 30 m height bins and 280 m along-track bins. Cloud-based ground detection flags are derived in the atmospheric data products ATL04 and ATL09 and tell us whether the Earth's surface is observable in a given location at a given time (Palm et al., 2019; Herzfeld et al., 2020). Surface data are telemetered only for a narrow range interval around an on-board Digital Elevation Model (DEM), where the size of the interval depends on surface height variability of the DEM.

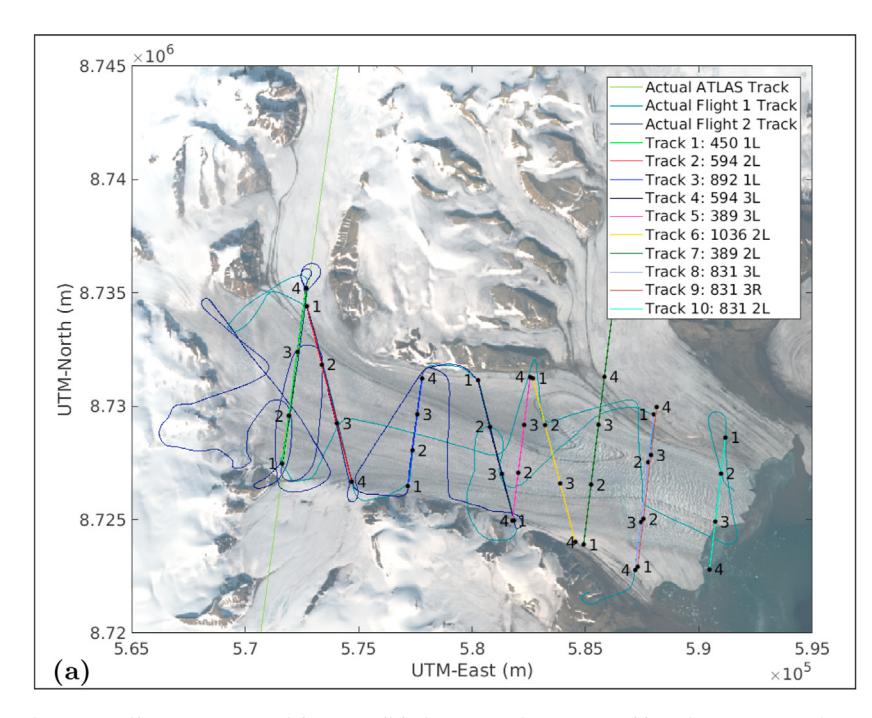
## 2.3. Orbit, multi-beam pattern and sampling geometry

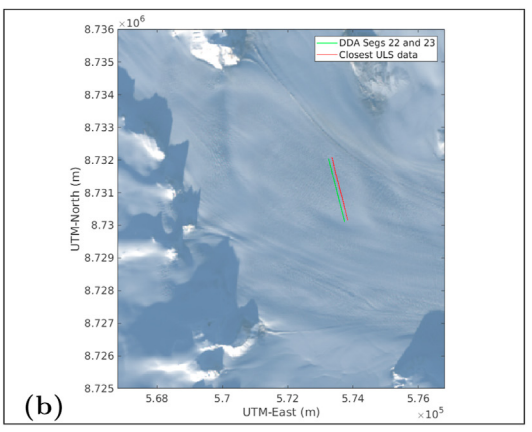
## Orbit

ICESat-2 has an orbit inclination of  $92^\circ$ , resulting in coverage of the Earth between  $88^\circ N$  and  $88^\circ S$ , and is operated on a 91-day exact repeat cycle. Reference ground tracks (RGTs) for the ICESat-2 mission have been determined prior to launch.

## Multi-beam pattern

ATLAS has 6 beams, organized in three sets of two beams, with a strong beam and a weak beam per set. Transmit energy of a weak beam is a quarter of that of a strong beam. Strong beams have 16 channels, weak beams have 4 channels (see Fig. 3). Weak beams are employed as a means





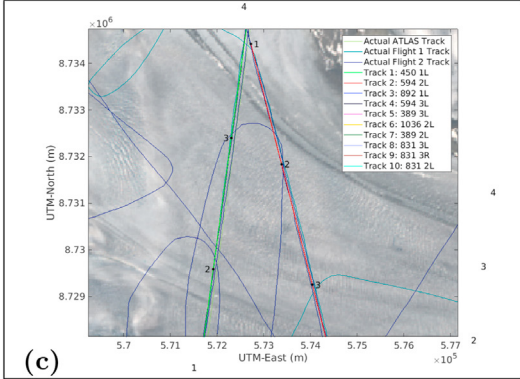


Fig. 2. Negribreen ICESat-2 Airborne Validation Campaign 2019 and location maps. Combining observation of the surge of Negribreen, Svalbard, with airborne evaluation of ICESat-2 data: (a) Planned and actual flight tracks and ICESat-2 ground tracks. Flight 1, 2019-Aug-12; Flight 2: 2019-Aug-13; Background: Landsat-8, 2019-Aug-05. (b) Location of airborne altimeter data (ULS data) used in comparison. (c) Zoom into (a).

to compromise between the goal of spatial coverage, originally addressed as cross-track surface slope determination, and the constraint of total energy available for laser signal transmission. Yawing of the transmitter array in a small angle relative to flight direction results in a 90-m across-track separation and a 2.5 km (5  $\pm$  0.2  $\mu$ rad) along-track separation of the weak and strong beams within the same pair. Across-track separation of two neighboring beam pairs is 3.3 km (6.61  $\pm$  0.26  $\mu$ rad) from the (idealized) center track of a beam pair to the (idealized) center track of the next beam pair, measured normal to flight direction. The observations follow a RGT, with the beams of the central pair falling to the left and right of the RGT. There are a total of 1387 RGTs.

### Sampling geometry. ATLAS flying forwards — ATLAS flying backwards

The transmitter array can be rotated and is operated as "ATLAS flying forwards" and "ATLAS flying backwards", which is changed approximately every 6 months, driven by the sun angle relative to the solar arrays (see, Fig. 3). Naming conventions are listed in Table 1. The array is rotated by a yaw angle of 2.06° with respect to flight direction (RGT) to create an offset of the ground tracks of the weak and strong beams in a pair by 90 m in the across-track direction. De facto, the transmitter array is continuously adjusted with respect to the actual flight direction, which requires 3-dimensional attitude corrections, of which yaw is the main component and the value of 2.06° is the time-averaged median. Reference pair tracks are at a fixed, nominal distance of 3.3 km in across-track direction from the RGT and pair track 2 is the same as the RGT. The actual pair tracks split the difference between the ground tracks of the weak and strong beams in each pair. Notably, the RGT falls between gt2l and gt2r by design. In contrast, for ICESat observations with the Geoscience Laser Altimeter System (GLAS), the observed altimeter data could fall to the side of the RGT. Required pointing accuracy is 800 m (i.e. the ground track point has to be within 800 m of the RGT). Along-track

separation of 2.5 km is also measured with respect to the RGT, i.e. in a direction parallel to the RGT.

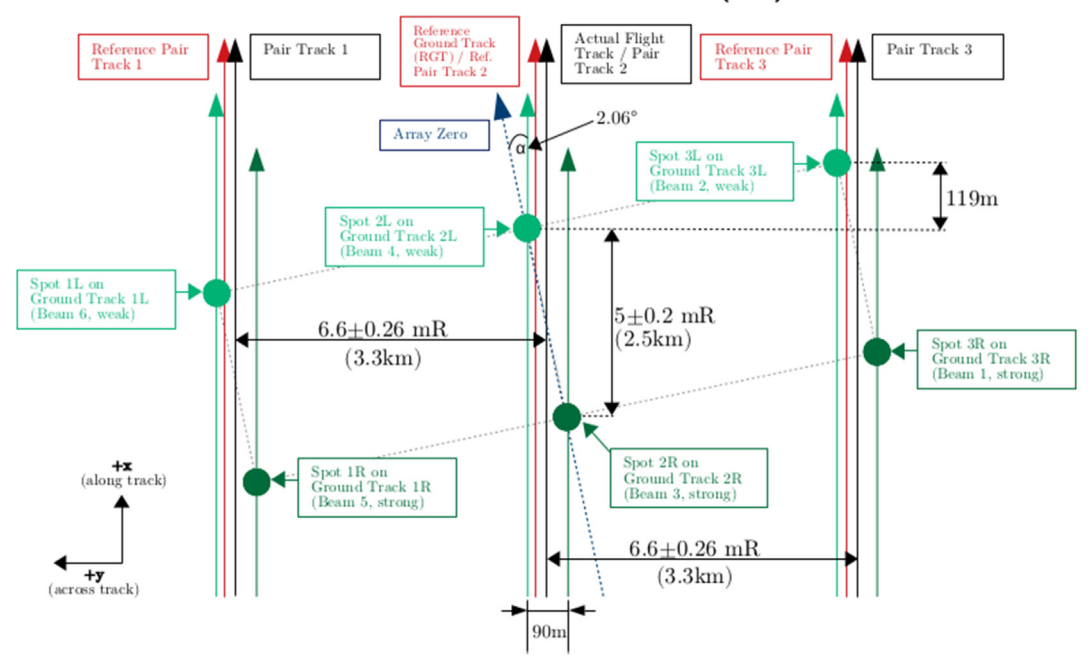
## 2.4. Geolocation and geophysical corrections

### Geolocation

The result of the geolocation process is the association of latitude, longitude and height (relative to WGS84) for each telemetered photon event in the point cloud. Geolocation of photon events relies on Precision Pointing Determination (PPD) of the laser and Precision Orbit Determination (POD). The ATLAS system has a Laser Reference System (LRS), two GPS antennas and Spacecraft Star Trackers to facilitate this.

Position determination of the ICESat-2 observatory uses the GEODYN platform (Luthcke et al., 2003), already employed for the ICESat Mission and several other missions. According to early analysis, the position of the center of mass of the ICESat-2 observatory is known to better than 3 cm radially. The geolocation algorithm uses two-way travel-time of the photon (light), transmit time of the laser pulse, spacecraft position and velocity, spacecraft attitude, in an Earth Centered Inertial (ECI) coordinate frame. Atmospheric refraction affects the determination of the so-called photon bounce point, this is solved in a first approximation and then iterated. Location of the bounce point is transformed from the ECI coordinate system into a an Earth Centered Fixed (ECF) coordinate system, accounting for precession, nutation, spin and polar motion of the Earth. Finally, the bounce point is given in the International Terrestrial Reference Frame (ITRF (Petit and Luzum, 2010),) as latitude, longitude and height w.r.t. the WGS-84 (G1150) ellipsoid based on ITRF 2014 constants ( $a_e = 6,378,137$  m,  $\frac{1}{f} = 298.257223563$ ). Geolocation is refined then taking into account refraction correction and tropospheric delay parameters. For reasons of computational efficiency, these operations are not carried out for every single photon, but for one photon per

# ATLAS oriented forwards (+x)



# ATLAS oriented backwards (-x)

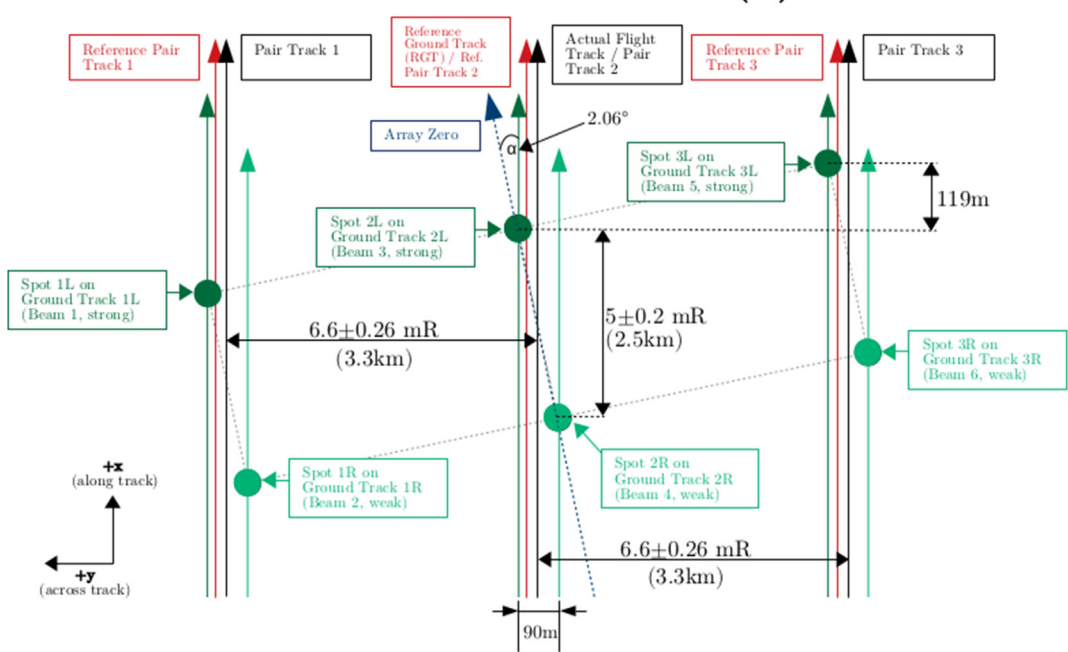


Fig. 3. ICESat-2 beam pattern and track geometry. For observatory orientations of ATLAS flying forward ("weak beams leading") and ATLAS flying backward ("strong beams leading"). Modified after (Markus et al., 2017), Fig. 2 and (Neumann et al., 2019a), Fig. 8. Beam numbering is a feature of the transmitter array, while spot and ground track numbering is a feature of the ATLAS data products, see Table 1.

approximately 20-m along-track segment, termed reference photon. That photon is selected following a criterion for high-confidence likely signal photons derived in ATL03, and if no such photon is found, a lower-confidence signal photon is selected, or a background photon. The algorithm for signal-photon identification and associated high, medium and low confidence is described in (Neumann et al., 2019b) (see also Section 7). All other photons in the same segment are geolocated using the reference photon's geolocation. For details on geolocation, the reader is referred to (Luthcke et al., 2000, 2002, 2005) and the ATBD for Receive-Photon Geolocation ATL03g (Luthcke et al., 2019).

## $Geophysical\ corrections$

Globally defined geophysical corrections are applied to the geolocated photon heights to allow comparison of height measurements at different times and with those of other data sources. The geophysical corrections include solid Earth tides  $H_{SET}$ , ocean loading  $H_{OL}$ , solid earth pole tide  $H_{SEPT}$ , ocean pole tide  $H_{OPT}$  and wet and dry atmospheric delays as total column atmospheric delay correction  $H_{TCA}$ . These corrections have been applied to photon height  $H_P$  above WGS84 in the ATL03 product and yield corrected photon height  $H_{GP}$  as

**Table 1** Identifiers for ATLAS orientations.

ATLAS Flying Forwards							
PCE	Strength	ATLAS Spot	Pair	GT	ATL03 Beam	ATL04/09 Atmosphere	Orientation
1	Strong	1	Right	gt3r	5	profile_3	1
1	Weak	2	Left	gt3l	6	profile_3	1
2	Strong	3	Right	gt2r	3	profile_2	1
2	Weak	4	Left	gt2l	4	profile_2	1
3	Strong	5	Right	gt1r	1	profile_1	1
3	Weak	6	Left	gt1l	2	profile_1	1

**ATLAS Flying Backwards** 

PCE	Strength	ATLAS Spot	Pair	GT	ATL03 Beam	ATL04/09 Atmosphere	Orientation
1	Strong	1	Right	gt1l	5	profile_1	0
1	Weak	2	Left	gt1r	6	profile_1	0
2	Strong	3	Right	gt2l	3	profile_2	0
2	Weak	4	Left	gt2r	4	profile_2	0
3	Strong	5	Right	gt3l	1	profile_3	0
3	Weak	6	Left	gt3r	2	profile_3	0

$$H_{GP} = H_P - H_{SET} - H_{OL} - H_{SEPT} - H_{OPT} - H_{TCA}$$
 (1)

but are identified on the product, so that they can be removed by the user. ATL03 also gives reference parameters to the EGM2008 geoid (Neumann et al., 2019a).

## 3. Method: the DDA-ice

### 3.1. Motivation and algorithm philosophy

The approach developed for determination of surface heights over crevassed and other morphologically complex terrain is the density-dimension algorithm for ice surfaces, the DDA-ice. This approach has been developed specifically for analysis of ICESat-2 ATLAS data, but it is generally valid for micro-pulse photon-counting laser altimeter data. The approach is introduced in (Herzfeld et al., 2017).

While the returned laser signal over a smooth ice surface is strong and easy to detect, the differences in surface morphology and surface material that exist across the Greenland and Antarctic ice sheets, across mountain glaciers, ice shelves and sea ice result in many different types of returns with different statistical properties. A simple histogram-based algorithm can typically not identify the surface height, if the surface is rough, for example, crevassed, and sometimes in cases of different materials (snow versus firn versus water on ice) (Herzfeld et al., 2014a, 2017). Examples of morphologically complex ice-surface types include crevassed surfaces, sastrugi fields, ridges and rubbled sea ice and regions with melt ponds in land ice and sea ice, to name a few. The regions where morphologically complex ice-surface types occur are important indicators of dynamically or climatically induced change processes and thus regions of interest in cryospheric research. Crevasses are surface signatures of glacial acceleration, as they form when the deformation forces exceed a threshold (Trantow and Herzfeld, 2018). A height-determination algorithm is needed that automatically adapts to changes in surface roughness and works for surface features of different scales.

The density-dimension algorithm was developed as a solution to these problems. It also adapts automatically to changes in signal-noise characteristics, including those caused by changes in ambient light during day-time and night-time, apparent surface reflectance and instrument effects. The surface height determined by the DDA-ice is not affected by a potential after-pulse in the signal, because the after-pulse is weaker (less dense) than the main surface signal. Thus a correction for after-pulse is not necessary (as opposed to the ATL06 algorithm, which needs a correction (Smith et al., 2019a; Smith et al., 2019b)).

The main idea of the DDA-ice is that signal photons can be expected to have a neighborhood with a higher photon density than background photons. To quantify density, photons are aggregated using a Gaussian radial basis function *(rbf)*. A *rbf* is a real-valued function whose value

decreases with distance from the center c:

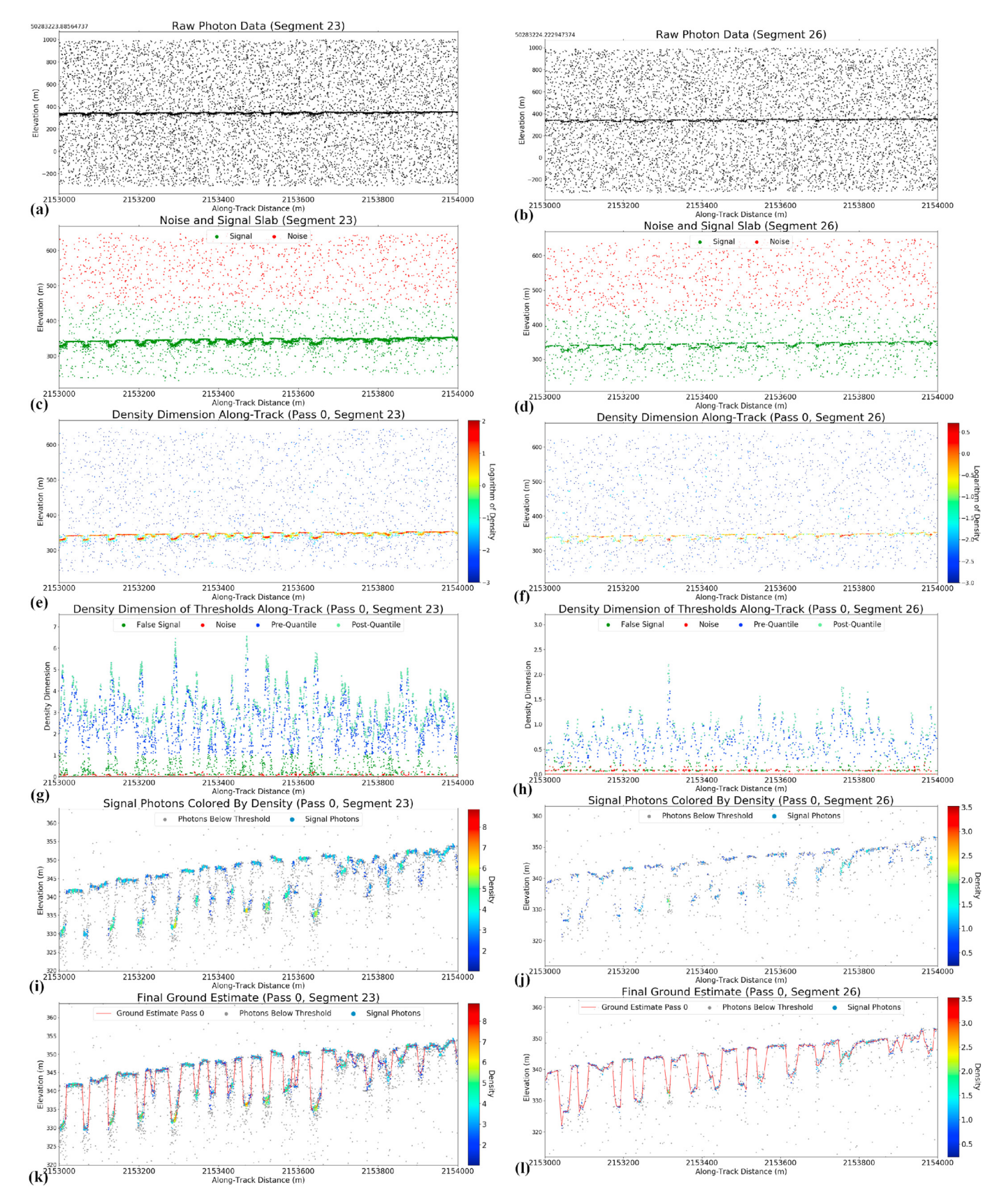
$$\Phi(x,c) = \Phi(||x-c||) \tag{2}$$

for all x in a definition area  $\mathcal D$  with respect to any norm  $\|\cdot\|$ . The density field of the photon cloud is calculated by letting each single photon take the role of a center, evaluating the  $\mathit{rbf}$  for all neighboring photons and forming the sum of weights from this process (Herzfeld et al., 2017). Signal photons are separated from noise photons using an auto-adaptive threshold function in the density domain.

## 3.2. Algorithm steps of the DDA-ice

The DDA-ice proceeds in several steps, described in the sequel. Most steps in this section have been mathematically defined in (Herzfeld et al., 2017) and tested using airborne altimeter data collected with the Slope Imaging Multi-polarization Photon-counting Lidar (SIMPL) (Dabney et al., 2010; Harding et al., 2011; Yu et al., 2016) over Greenland ice surfaces in 2015, prior to launch of ICESat-2. SIMPL is a dual-color (532 nm, 1064 nm), dual-polarization (parallel-polarized, orthogonal-polarized) multi-beam lidar and can be considered an airborne simulator instrument for ATLAS. Now the DDA-ice is applied to ICESat-2 ATLAS data collected from space. The steps are illustrated in Fig. 4 for ATLAS data collected over Negribreen on 2019-August-05 (RGT594), with the left column illustrating results for the strong beam.

- (1) Separation of noise and signal slabs. Prior to the density calculation, the approximate height of the surface is determined using large-scale histograms, calculated for large along-track bins. This step identifies a signal slab and a noise slab. The signal slab is a height interval defined around the histogram maximum, typically  $\pm 100\,\mathrm{m}$  resulting in a 200 m signal slab. The noise slab is then defined as the slab of the same thickness (height interval of the same size, here 200 m) above the signal slab. For a 1-km segment of raw photon data (Fig. 4a), the signal slab and the noise slab are shown in Fig. 4c.
- (2) Cloud avoidance operators. Noting that the surface signal can be obscured by clouds, a cloud-avoidance operator is introduced. The concept of this operator is to discriminate the cases where the height slab with the strongest histogram is an atmospheric layer and where the strongest signal is actually returned from ground. Several options for cloud-avoidance operators have been developed, one of those is described in (Medley, 2016). The cloud avoidance operator is not tied to the DEM (digital elevation model derived from other sensors and information sources), to not compromise the capability to detect large elevation change signals with ICESat-2. In the data analysis described here, the default histogram step is used, because data were collected under



(caption on next page)

Fig. 4. Steps of the DDA-ice algorithm for a crevassed region in upper Negribreen. [ATL03\_20190805232841\_05940403\_002\_01.h5] [RGT 594 gt1l, strong beam [left column] and RGT 594 gt1r, weak beam [right column], collected 2019-Aug-05, 23:28 GMT = 1:28 local time, night-time/low twilight data]. Segment 23 for strong beam matches segment 26 for weak beam, because along-track separation is 2.5 km, and across-track separation is 90 m, see Fig. 3. (a), (b) Raw data (photon point cloud) from ATL03. (c), (d) Signal slab (green) and noise slab (red) for a slab thickness of 200 m. (e), (f) Density field. (g), (h) Application of auto-adaptive threshold function in density space. Illustration of the autoadaptive threshold function that is the core of the density-dimension concept. Density values in red stem from photons in the noise slab. The threshold offset is an additive value that ascertains separation of signal and noise photons based on their density values. Cyan points stem from photons in the signal slab that are below the first threshold value. Blue and green points are the points for which the quantile is formed. The separation of green points and blue points near the top indicates the separation of signal and noise photons. (i), (j) Height of signal and noise photons with density. Location of photons identified as signal is plotted with density indicated by larger, colored disks, with density coded by color. Points identified as noise-return and filtered out are plotted as small, grey disks. The identification of ground returns results from the step illustrated in panels (g, h). (For more explanations, see also (Herzfeld et al., 2017)). (k), (l) Height of signal and noise photons with density and roughness-adaptive ground follower. These panels illustrate the autoadaptive ground-following algorithm (thin red line). Photons plotted as in (i), (j). (For interpretation of the references to color in this figure legend, the reader is referred to the Web version of this article.)

- clear-sky conditions (i.e. the cloud avoidance operator is not applied).
- (3) Calculation of the rbf for each photon to create the density field. Letting each photon in the signal slab and the noise slab take the role of a density center, the density field is calculated by evaluating the radial basis function, as introduced in Eq. (2). For an exact mathematical definition of this operation, the reader is referred to (Herzfeld et al., 2017). The radial basis function can be visualized as a Gaussian function that rotates around a vertical axis, forming a bell-shaped body with circular isolines at each density level.

The radial basis function has a kernel, which is controlled by the algorithm-specific parameters standard deviation  $\sigma$  (in meters), cutoff u (defined as the number of standard deviations used to delimit the kernel) and anisotropy  $\alpha$ , which turns the circular bell shape into an ellipsoidal one. Using  $h_1$  for the horizontal axis of the kernel ellipsoid and  $h_2$  for the vertical axis,

$$h_2 = \alpha h_1 \tag{3}$$

An anisotropic kernel is employed, because there is a higher probability of finding neighboring ground points in the horizontal direction than in the vertical direction, thus for most surfaces  $\alpha>1$  is used. For crevassed surfaces,  $\alpha<1$  may be applied. Here we employ  $\alpha=1$ , because the tracks cross crevassed and uncrevassed terrain. The sensitivity of the DDA-ice results to changes in the algorithm-specific parameters, given in Table 2, is demonstrated in (Herzfeld et al., 2017). The resultant density field is visualized in Fig. 4e.

Table 2
DDA-ice parameters. Strong beam, weak beam - ATLAS beams. Parameters used for strong beam are the same as parameters optimized for analysis of SIMPL\_green (532 nm parallel polarized) channels. Variables Q and S are now algorithm-specific parameters for DDA-ice, but were fixed parameters for SIMPL\_green data analysis with the same values (Herzfeld et al., 2017).

symbol	meaning	strong beam	weak beam
		ATLAS(actual)	ATLAS(actual)
S	standard deviation	3	4
u	cutoff	1	1
a	anisotropy	1	1
q	threshold quantile	0.5	0.6
k	threshold bias offset	1	0.2
1	slab thickness (m)	200	200
R	resolution of ground follower (m)	5	5
r	factor to reduce the R parameter	2	1
-	resolution of ground follower for rough surfaces (m)	2.5	5
Q	crevasse depth quantile	0.5	0.5
S	standard deviation threshold of thresholded signal to trigger small step size in ground follower (m)	1.75	1.75

(4) Auto-adaptive threshold function. An auto-adaptive threshold function is applied to separate noise and signal photons, using density as an additional dimension. The concept of this function is to use the statistical properties of the photons in the noise slab compared to those of the photons in the signal slab, to separate signal from noise photons. It is important to note that the signal slab contains both signal photons and background photons, whereas the noise slab contains only background photons. There are a few exceptions to this rule, because part of the signal could be attenuated by near-ground atmospheric effects in the noise slab, and instrument artifacts can disturb the simplicity of this concept. Therefore, an auto-adaptive threshold function is introduced rather than a simple quantile. The operation of the threshold function is visualized in Fig. 4g and the resultant signal photons are shown in Fig. 4i, colored with density.

The auto-adaptive capability of this function is an essential ingredient of the DDA, as the absolute photon density is much larger during daytime than during night-time, it also varies with apparent surface reflectance (ASR), which is especially significant over ice surfaces. Step 4 yields surface height for each photon in the signal set, and all photons have been geolocated in ATL03 (prior to DDA-ice application), as described in Section 2. Several algorithm-specific parameters control the threshold function, including threshold quantile and threshold-bias offset (for mathematical definitions, see again (Herzfeld et al., 2017)).

- (5) Ground follower, (a) simple and (b) auto-adaptive to surface roughness. The surface-height determination is complete with step 4, however, for some applications it is advantageous to provide interpolated surface height as a line. To this end, a ground follower is introduced. A piece-wise linear function, weighted by density, is selected, because it makes minimal assumptions about the local shape of the surface, leaving this to spatial distribution of the photons in the local signal set.
  - (5a) Simple ground follower. The simple ground follower employs a piece-wise linear function with a fixed bin-size, R, that is weighted by density in the signal set.
  - (5b) Crevasse identification and crevasse measurement using a roughness-adaptive ground-follower. The ground follower automatically switches between two options, one for smooth, or uncrevassed, surfaces, and one for rough, typically crevassed surfaces. Roughness of the surface at a level indicative of crevasse existence is determined based on the standard deviation s of the height component of the signal photons in the bin. If  $s > s_{rough}$  for a threshold parameter  $s_{rough}$ , then the surface is determined to be rough and the crevasse-detection module of the algorithm kicks in. The  $s_{rough}$  parameter has the description "Standard deviation threshold of thresholded signal to trigger small step size in ground follower (meters)". In the analysis in this paper,  $s_{rough} = 1.75$  m is used. In the crevasse-detection module, the

ground follower is refined by dividing the segment-length R of the ground follower by a factor r to increase resolution. For example, if the ground-follower resolution is R = 5 m for uncrevassed terrain and the ground follower refinement factor is r = 2, the ground-follower resolution for crevasses is R = 2.5 m. The analysis in this paper employs the roughness-adaptive ground follower for all data sets. Notably, the roughness-adaptive ground follower performs well for smooth surfaces as well (see Fig. 5). In other applications, the ground follower is used with 1-10 m resolution over smooth surfaces and 0.5-5 m over crevasses or sastrugi (rough surfaces). Fig. 4i shows the photons that are identified as ground returns, with their associated density values in color, at the surface height given in ATL03. These signal photons include those returned from crevasse bottoms or along crevasse walls. Spacing of the height measurements in the set of signal photons is nominally 0.7 m. De facto, it is the same as given by the photon cloud, because no averaging has been performed. The roughness-adaptive ground-follower shows surface height for a continuous line through the signal photons (Fig. 4k).

### 3.3. Algorithm-specific parameters

The DDA-ice is controlled by a set of algorithm-specific parameters. These parameters are mathematical variables that are programmed as numerical variables in the computer code and assume specific values for a given class of data analysis. Specific values for a data analysis, here, for ICESat-2 post-launch data, are determined in an analysis of the sensitivity of DDA-ice results to changes in the algorithm-specific parameters (sensitivity study). There are several advantages to this computational approach: First, the instrument characteristics of the ICESat-2 ATLAS sensor are expected to change throughout the mission. For example, at launch the energy level of the sensor was set to a value of 6, but later changed to a value of 4. As the mission goes on, the energy level of the instrument is likely to drop (as was the case for the GLAS instrument of ICESat, see e.g. (Herzfeld et al., 2014b)). Signal-to-background characteristics can also change. To match algorithm performance to resultant changes in data characteristics, it is only necessary to perform a sensitivity study and adjust the parameters (as opposed to redesign the code). At this point, a sensitivity study requires extensive experience in the algorithm's performance. Once the parameters are set, the algorithm is auto-adaptive to several things, as described in the previous sections. Second, the DDA-ice is generally applicable to analysis photon-counting lidar altimeter data and the use of algorithm-specific parameters increases the class of sensors whose data can be processed with the DDA-ice.

The analysis in this paper uses the following algorithm-specific parameters (Table 2).

The parameters for the strong beam are similar to those used for the analysis of green parallel-polarized data from SIMPL in the pre-launch airborne simulator campaign (Herzfeld et al., 2017). This indicates that the 532 nm parallel-polarized channels of SIMPL sensor performed very similar to post-launch ATLAS data and also speaks for the adaptability of the algorithm, the DDA-ice. The algorithm has been generalized to allow different values for the crevasse quantile and for the roughness-adaptive ground follower, upgraded from the version used in (Herzfeld et al., 2017) for SIMPL data analysis. A sensitivity study for SIMPL 532 nm data is given in (Herzfeld et al., 2017).

## 3.4. Characteristics of the DDA-ice

The DDA-ice has the following characteristics:

 Input: Geolocated photon point cloud in ATLO3. The DDA-ice builds on the geolocated photon point cloud provided in ATLO3 (signal

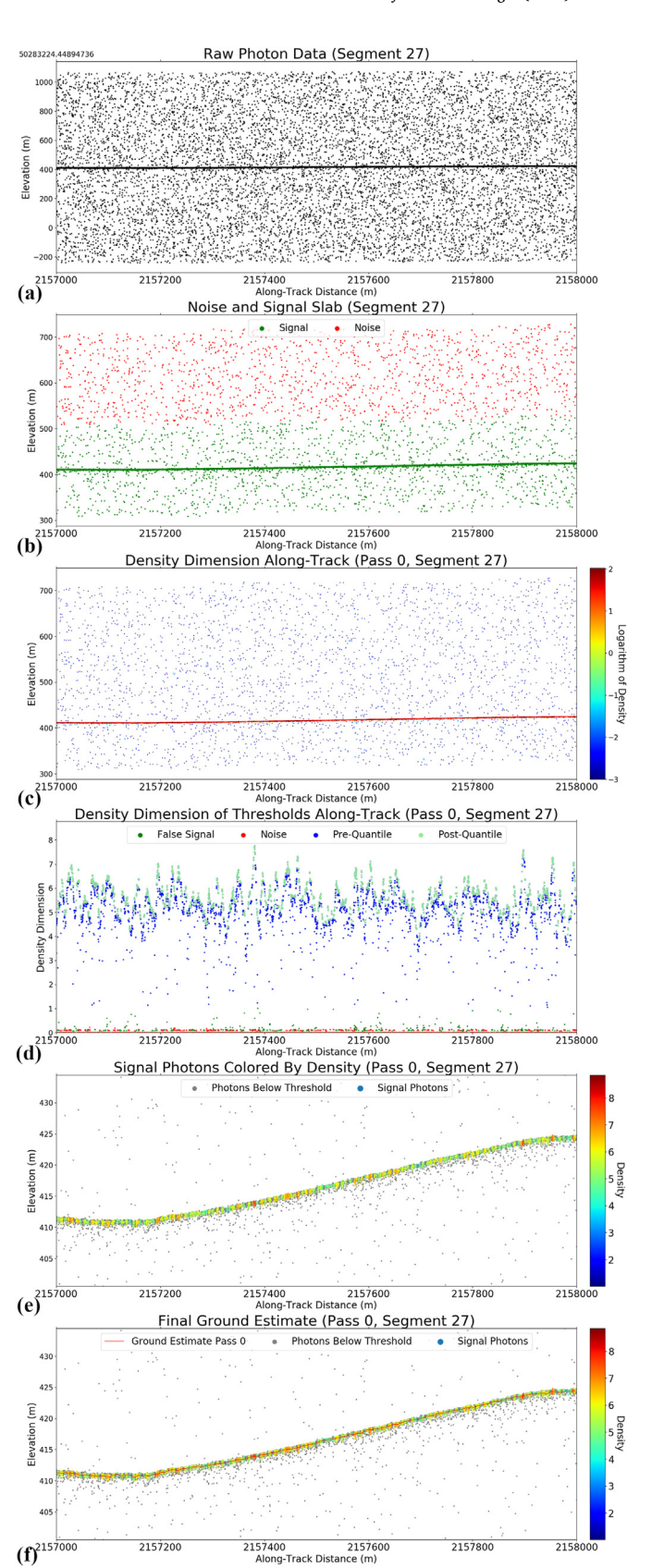


Fig. 5. Steps of the DDA-ice algorithm for a smooth region in upper Negribreen. [ATL03\_20190805232841\_05940403\_002\_01.h5] [RGT 594 gt1l (strong beam), collected 2019-Aug-05]. Steps as described in caption of Fig. 4.

and noise/background photons). It is worth noting that the DDAice does not utilize the photon classification reported in ATL03 (Neumann et al., 2019b).

(2) The DDA-ice resolves surface heights at the resolution of the point-cloud data (nominally 0.7 m along-track).

Because the density field is calculated with each individual photon acting as a density center (in step 3) and the threshold function classifies signal photons (step 4), surface heights are determined at the resolution of the sensor. Neither step 3 nor step 4 reduces spatial resolution, the DDA-ice is a data aggregation and not a data averaging method. The resolution of the point cloud data is preserved in the analysis. The ground follower is implemented as a piece-wise linear interpolation of the signal photon set, with bin sizes that can be adjusted. Here we use 5 m for smooth surfaces and 2.5 m for crevasse interiors and crevasse edges, and generally for rough surfaces. For comparison, the ATL06 data product resolves surface height in 40-m segments with 20-m postings (see, Section 7).

- (3) The DDA-ice resolves crevasses and other morphologically complex surfaces. The DDA-ice measures crevasses, with the ground follower following surface height into and out of crevasses. This allows characterization of several different crevasse types, as will be illustrated in this paper.
- (4) The DDA-ice works for surface height determination from weak beams as well. This is exemplified in Section 4.4.

# 4. Application of the DDA-ice to ICESat-2 ATLAS data from Negribreen, Svalbard, during surge

# 4.1. Survey area of Negribreen, experiment setup, instrumentation and geolocation

Negribreen, one of the largest glaciers in Svalbard, has been surging rapidly in 2017 and 2018, accelerating to 200 times its normal velocity, an event that last occurred in 1935/36 (Lefauconnier and Hagen, 1991) (see Fig. 1b). The surge of Negribreen has provided an unusual opportunity to collect validation data for ICESat-2 over crevassed and complex ice surfaces, because (a) the surge dynamics leads to rapid changing of the ice surface, especially through crevassing and increased water presence (due to changes in the hydrological system of a surge glacier during the active surge phase) and (b) many different ice surface types exist in close proximity, which allows for time and cost efficient sampling of surface types.

We conducted two ICESat-2 airborne validation campaigns over the surging Negribreen, Svalbard, in July 2018 and August 2019, collecting airborne laser altimeter data, image data and kinematic Global Positioning System (GPS) and Inertial Measurement Unit (IMU) data. In 2018, flight tracks followed the location of the future ICESat-2 reference ground tracks. The 2019 Negribreen ICESat-2 validation campaign combined the objectives of observing the surge with evaluation of (postlaunch) ICESat-2 data. To optimize the return of useful data from limited flight hours possible in challenging Arctic weather conditions and constrained by cost, flight tracks were planned and selected using (a) locations of tracks from the 2018 campaign, (b) information on clear-sky ATLAS data collected in days preceding the field campaign (provided by the ICESat-2 project), (c) coverage for each of the six ATLAS beams, and (d) distribution of crevasse provinces and surface characteristics in the field. A map that combines planned and actual flight tracks and ICESat-2 tracks is shown in Fig. 2. Data used in this paper stem from 2019-Aug-12 (flight 1) and 2019-Aug-13 (flight 2).

The following data were collected:

 Surface height and spatial surface roughness characteristics: Laser altimeter data [Universal Laser System, ULS, LaserTech], 905 nm, 4000 Hz internally, 400 Hz output, 3 mrad beam divergence (30

- cm footprint at 100 m range), 200–300 m agl,  $\approx$  0.12 m point spacing (Crocker et al., 2011).
- (2) Surface classification and deformation analysis: Nadir-pointed timelapse imagery at 2 images per second (GoPro Hero5, linear setting)
- (3) *Geolocation:* Kinematic GPS data, using a base station placed on the side of Negribreen (Trimble NetR9) and a rover mounted on the helicopter (Trimble Polar R10)
- (4) Attitude correction: Inertial Measurement Device (IMU) data (LORD strainmeter)
- (5) Documentation: Photography (NIKON D5100)

Analyses in this paper are based on differentially (kinematically) corrected GPS locations, with IMU correction applied. In 2018, experiments in real-time kinematic (RTK) data collection and analysis were carried out in addition, with the conclusion that differential (kinematic) data collection and analysis is most efficient in practice and yields the most accurate repeats of the ICESat-2 ground tracks (better than RTK for a number of reasons). Resultant separation between ATLAS ground tracks and airborne ground tracks is better than 20 m and generally within a few meters for the 2019 data analyzed here (Fig. 2b and c). The geodetic aspects of the ICESat-2 validation campaigns are treated in detail in a companion paper (Herzfeld et al., Lawson). In this paper, we focus on the surface-height determination, using ATLAS data and the DDA-ice.

### 4.2. Crevasse characteristics of a surging glacier

The DDA-ice is applied to analyze ICESat-2 ATLAS data from RGT594 (see, Fig. 2a and Table 3), as explained in Section 3.2. The resultant signal photons stem from the ice surface between crevasses, from crevasse walls and from crevasse bottoms. The surface follower and the signal-photon set portray the morphological characteristics of freshly opened crevasses of a surging glacier (Fig. 4i, also Fig. 4Xa): Clear-cut crevasses with little roundedness of crevasse edges, indicative of relatively recent opening. The roundedness parameter is introduced in (Herzfeld et al., 2013), it increases as crevasse edges are exposed to weathering, snowfall, melting and wind deposition and erosion. Although the total photon count is much lower for the matching segment of the weak beam (segment 26, Fig. 4l and 4Xb, in supplement), the same characteristics are also evident from the weak-beam analysis. Crevasses within a homogeneous surface province have a regular spacing (2153000–2153600 m along-track in Fig. 4i and 4Xa, in supplement).

Fig. 5 illustrates that the DDA-ice works equally well for a smooth, uncrevassed region. It is a property of the auto-adaptive algorithm that it functions for crevassed and smooth surfaces without supervision or intervention from a user, using the same set of algorithm-specific parameters, listed in Table 2. The algorithm has several auto-adaptive components that help the algorithm "decide" whether it is analyzing a smooth or a rough surface and what segment lengths to use for the ground follower. Close scrutiny of the resultant figure panel (Fig. 5e) shows that the signal photon set excludes photon returns that are scattered below the surface. Furthermore, the random distribution of subsurface photons provides additional illustration of the differences in spatial characteristics between photons returned from crevasses below

Table 3
Crevasse spacing and depths for Negribreen evaluation profile "segment 23 (RGT594) 2019–Aug–05". Comparison of results from ULS airborne laser altimeter data and DDA-ice applied to ICESat-2 ATLAS data ATL03\_20190805232841\_05940403\_002\_01.h5.

	Mean CrevasseSpacing (m)	Maximum CrevasseDepth (m)	Mean CrevasseDepth (m) (> 5 m)
DDA- ice	52.12	16.01	10.95
ULS	58.82	13.96	10.18

Table 4

ICESat-2 granules used in analysis in this paper. "Beam" lists strong beams. Matching weak beams are also analyzed. Orientation refers to the orientation of the ATLAS instrument array (Table 1). Data release r002.

Location	Granule Name	Date	RGT	Beam	Orientation
Negribreen	ATL03_20190727132129_04500405_002_01.h5	July 27, 2019	450	gt1l	Backwards
Negribreen	ATL03_20190805232841_05940403_002_01.h5	August 5, 2019	594	gt1l	Backwards
Jakobshavn	ATL03_20190511210825_06660305_002_02.h5	May 11, 2019	666	gt3l	Backwards

the main glacier surface and photons returned from within the ice. The relatively few background photon above the surface are statistically characterized by the set of red-labeled photons in the threshold plot (Fig. 5d), which allows to discriminate between the distribution of subsurface background photons and sub-surface returns from within the ice.

## 4.3. Validation using airborne laser altimeter data from the Negribreen-ICESat-2 campaign 2019

Selecting the same segment 23 as an example for the evaluation of the surface-height determination capabilities of ICESat-2 and the DDA-ice over crevassed terrain, we analyze ULS data in comparison to ATLAS data. A visual comparison is provided in Fig. 6. Because the ULS operates at 905 nm (NIR light), its signal interacts differently with the snow/ice/firn material at the surface of the glacier and inside the crevasses. Despite these differences between the NIR airborne sensor and the green-light ATLAS lidar, the two different crevasse provinces can be identified in both data sets, with a boundary between the two structural provinces crossed at along-track distance of 2153650 m approximately (in both the ATLAS and the ULS tracks). Table 5 summarizes spatial characteristics. Maximum and mean crevasse depths are similar, with depth

measurements of the ULS more shallow, as the green light penetrates further, while NIR light tends to reflect off the surface of snow/ice, especially in case of partial water saturation. Mean crevasse spacing is

Table 5

Jakobshavn Isbræ crevasse spacing estimates from DDA-ice results and SkySat imagery. Comparison of individual and mean crevasse spacings for segment 18, Fig. 8.

Segment	DDA-ice (m)	Skysat (m)	
1	59	58	
2	106	108	
3	82	83	
4	106	120	
5	82	83	
6	76	79	
7	100	100	
8	94	113	
9	65	71	
10	71	58	
11	53	42	
12	82	58	
Mean Spacing	81.37	81.25	

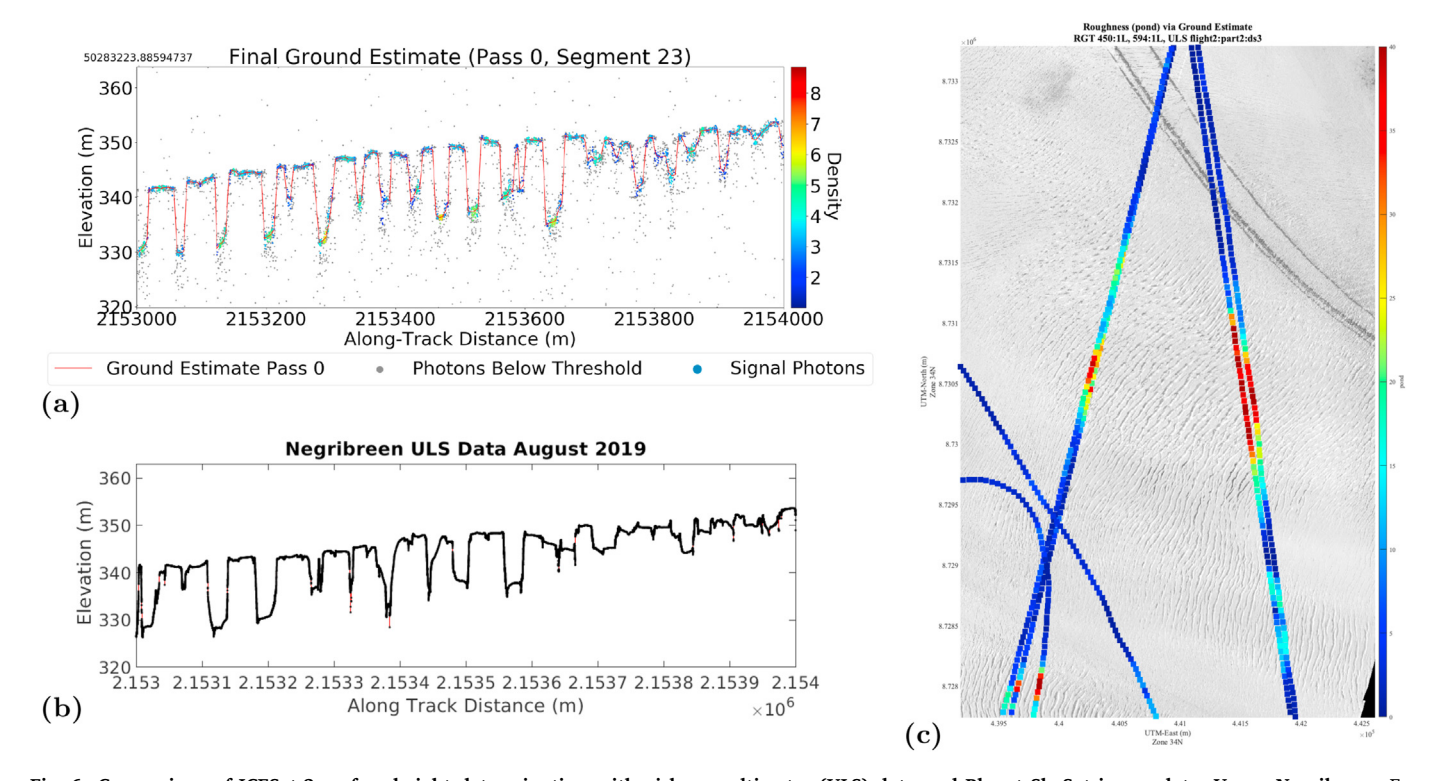


Fig. 6. Comparison of ICESat-2 surface-height determination with airborne altimeter (ULS) data and Planet SkySat image data. Upper Negribreen. For locations see Fig. 2a and b. ICESat-2 ATLAS Granules: [ATL03\_20190805232841\_05940403\_002\_01.h5] [RGT 594 gt1l 2019-Aug-05] and [ATL03\_20190727132129\_04500405\_002\_01.h5] [RGT 450 gt1l]. SkySat Image [20190818\_150858\_ssc9\_u0002\_panchromatic\_dn.tif]. SkySat ssc9 data have 0.72 m pixel size. (a) ICESat-2 ATLAS segment 23, strong beam. [ATL03\_20190805232841\_05940403\_002\_01.h5] [RGT 594 gt1l 2019-Aug-05]. (b) ULS surface heights from airborne campaign, collected 2019-Aug-13. (c) Roughness measure pond<sub>res</sub> calculated for ICESat-2 RGT594 (right) and RGT450 (left) and for ULS data. For RGT 594, the airborne track (ULS) is to the east (right) of the satellite track. For RGT 450, the airborne track and the satellite track are almost in the same location. See Fig. 2 for location details. Generally, surface roughness from parallel tracks and crossover locations matches between ICESat-2 and ULS. The pond<sub>res</sub> measure increases with intensity of crevassing evident in the SkySat image.

also similar (52.12 m for ATLAS and DDA-ice compared to 58.82 m for ULS data), the difference results from the detection of a single additional crevasse in the 1-km segment.

The differences in measurements of crevasse depths and crevasse spacing between the ICESat-2 data (532 nm) and the airborne validation data are a result of the different frequencies of the sensors (905 nm). An analysis comparing the apparent height differences resultant from altimeter measurements using 1064 nm red (NIR) and 532 nm green light of the SIMPL instrument is given in (Herzfeld et al., 2017), this difference is attributed to differences in firn penetration for the two frequency channels. The 905 nm ULS sensor is used in airborne campaigns because its classification as an eye-safe laser facilitates obtaining a permit for the laser's operation from an aircraft (see, Acknowledgements.) As the results show, the ULS measurements can be employed to evaluate ICESat-2 data regarding the existence and location of crevasses and their depth and spacing characteristics. In addition, geostatistical characterization can be applied (Section 5).

## 4.4. Weak-beam analysis

Fig. 4 (right column) illustrates that determination of surface height in crevassed terrain is possible not only from strong-beam returns, but also from weak-beam returns, using the DDA-ice. The total number of raw data in the photon point cloud is much less than for the strong beam (Fig. 4b). As described in Section 2 on the properties of the ATLAS instrument, the transmit strength of a weak beam is a quarter of that of a strong beam. The raw data set for the weak beam includes a similar number of background photons as that of the strong beam, which means that the signal-detection problem is even more ill-posed for the weak beam analysis. The figure panels of density-dimension (Fig. 4e and f) reflect the relationship of 4:1 in the density values of the surface-andcrevasse photons. The threshold function adapts to the smaller differences between signal and noise (Fig. 4h) and correctly identifies the signal-photon set (Fig. 4j). Different values are used for some of the algorithm-specific parameters (larger standard deviation, smaller threshold quantile and smaller threshold-bias offset; see Table 2).

The resultant ground estimate derived from the weak-beam data is remarkably similar to that of the strong-beam data, for both the spatial characteristics of the signal-photon set and the ground follower (Fig. 4l, 4Xb), given that the across-track separation of the weak and strong beam within a pair is 90 m. Because along-track separation is 2.5 km, segment 26 for the weak beam is compared to segment 23 for the strong beam. In summary, detection of crevasses and measurement of their depth is possible for both the strong beams and the weak beams.

## 5. Geostatistical characterization of surface roughness for different crevasse provinces of Negribreen calculated from ICESat-2 ATLAS data and airborne altimeter (ULS) data and compared to high-resolution satellite image (Planet SkySat) data

## 5.1. Planet SkySat data and synoptic visualization tool for ICESat-2 data

## Planet SkySat data

Planet (previously PlanetLab) is a California-based commercial satellite-data provider who launched several series of small satellites, including the SkySats. The Planet SkySats comprise a fleet of 15 small commercial satellites that are equipped with optical and near-infrared imaging systems. Earlier systems (ssc1 and ssc2) have a spatial resolution of 0.86 m pixel size, newer systems (ssc3 to ssc13) have 0.72 m pixel size, and all systems were in operation in 2019. These pixel sizes are close to the 0.7 m nominal along-track spacing of ATLAS data, thus SkySat imagery is well-suited to evaluate ICESat-2 data - and vice versa. In the framework of a NASA-led effort to assess commercial satellite imagery, we had the opportunity to task a special SkySat image acquisition for a number of glacier areas of interest, carried out in September and October 2019. SkySats can be tasked to collect imagery from space, the resultant

images are relatively small (Fig. 7). Images are of course affected by cloud cover. SkySat imagery was collected over Negribreen during the time of ICESat-2 airborne validation campaign, here we analyze an image from 2019-Aug-18 with 0.72 m resolution (ssc9) (Fig. 6c). The near-coincident imagery allows direct comparison with the ULS data (collected 2019-Aug-13) and the ICESat-2 data (RGT 594: 2019-Aug-05, RGT 450: 2019-Jul-27).

## ICESat-2 altimetry - SkySat imagery visualization tool

To facilitate visual and quantitative spatial comparison of SkySat image data and ICESat-2 data, we built a software tool for visualizing the SkySat data with the ICESat-2 actual ground tracks superimposed. This tool allows to (1) evaluate ICESat-2 surface-height determination over complex crevassed terrain, using SkySat imagery, and (2) derive a crevasse characterization.

## 5.2. Geostatistical characterization of crevasse provinces

Crevasses play an important role in observation, analysis and numerical modeling of ice dynamics. Crevassing occurs when a threshold in the kinematic forces resultant from glacial acceleration is exceeded and the material ice responds with brittle deformation (Herzfeld and Mayer, 1997; Mayer and Herzfeld, 2000; Herzfeld et al., 2014b; Trantow and Herzfeld, 2018). Crevasses form in fields of similar spatial characteristics with clear boundaries to neighboring fields, which motivates the introduction of the term "crevasse province" for a crevassed region that is maximal with respect to homogeneity of crevasse characteristics (Herzfeld et al., 2014b). Spacing and depth of individual crevasses are less important than the spatial characteristics of the province. The geostatistical characterization and classification method (Herzfeld, 2008) has been developed to provide quantitative parameters that summarize spatial properties of crevasse fields and can be directly related to numerical modeling (Trantow and Herzfeld, 2018).

In this context, we apply geostatistical characterization to both the ULS data and the ATLAS data collected over Negribreen and superimpose the results on a SkySat image of the ice surface of Negribreen during surge in August 2019 (Fig. 6c). This will serve as an additional mathematical evaluation of the ICESat-2 data and the DDA-ice and provide a context to surge dynamics. To this end, we calculate the first classification parameter, the  $pond_{res}$  parameter, as a measure of surface roughness. The pondres parameter is defined as the largest value in a first-order experimental residual vario function (Herzfeld, 2008). Here, geostatistical characterizations are derived from residual vario functions of the DDA-ice ground follower values with 5 m lag bins. Estimates are calculated within 300-m along-track windows and posted every 50 m along-track. The ULS data are down-sampled to 3 m resolution to better match the DDA-ice ground follower resolution of 5 m over flat terrain and 2.5 m over crevassed terrain (see, Table 2). The  $pond_{res}$  measure is then calculated for ULS data using the same controls (300 m along-track windows with 50-m offsets and 5-m unit lags in the vario-function calculation). Fig. 6c indicates three results: (1) Generally, surface roughness from ICESat-2 DDA-ice and ULS surface heights matches for coincident tracks and in crossover locations. (2) The value of the pond<sub>res</sub> parameter increases with intensity of crevassing evident in the SkySat image. Uncrevassed regions have low roughness values (dark blue colors). The province of deep crevasses with clear-cut edges typical of surging, seen in segment 23 (Fig. 6a and b), has the highest roughness values (red and dark red). Recently opened thin, near-parallel crevasses in the SE corner of the satellite image are characterized by intermediate roughness values (light-blue and green). (3) As best observed for the RGT 594 and parallel ULS tracks, roughness values are generally a little higher for the ICESat-2 data than for the ULS data, which can be explained by the fact that crevasse depths from 532 nm data are somewhat larger than from 905 nm data for physical reasons (see, Section 4.3). However, values from both ULS and ICESat-2 data fall in the same category and thus both serve to characterize the same crevasse classes. In conclusion,

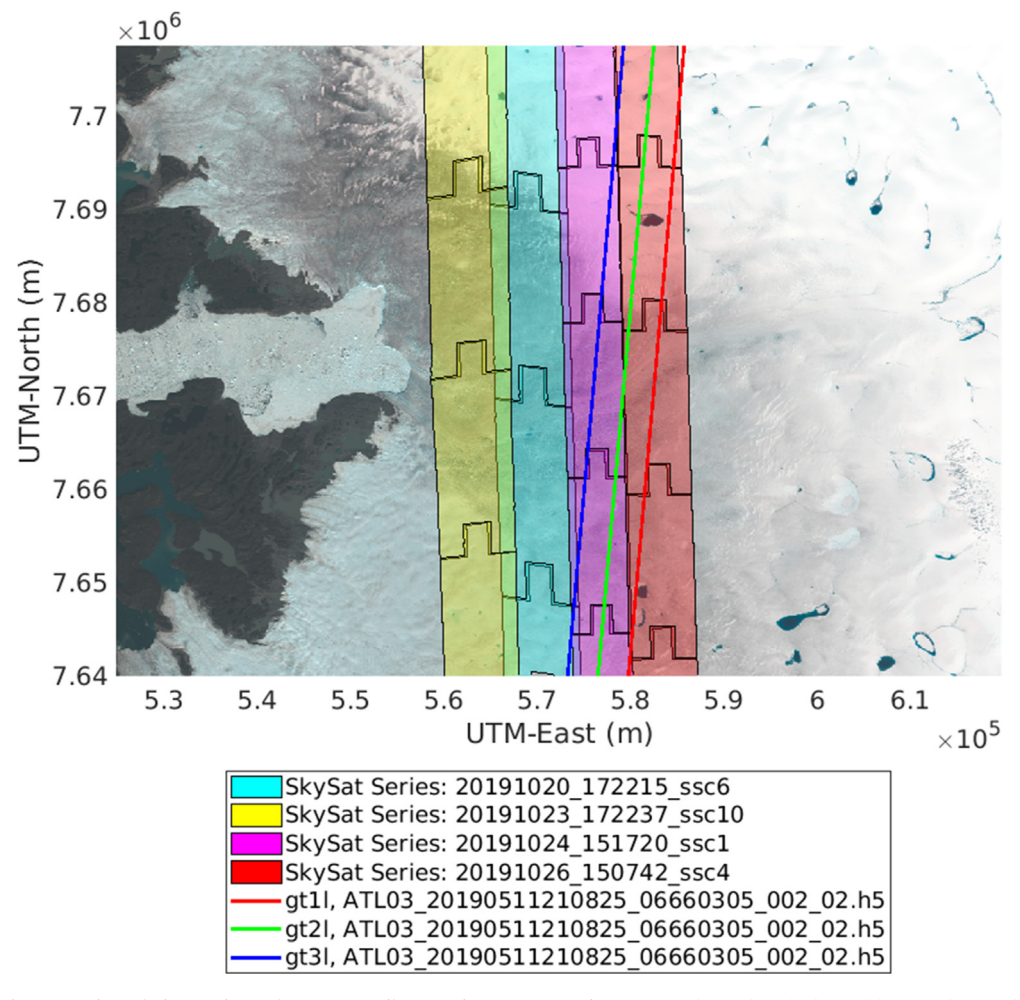


Fig. 7. Jakobshavn Isbræ, overlay of Planet Skysat imagery outlines and ICESat-2 tracks. Data used are identified in Table 3. Background Landsat-8 from 2018-Jul-30. For ATL03 from 2019-May-11, RGT 666. We use gt3r (strong beam) and gt3l (weak beam). ATLAS flying backwards.

comparison of roughness characterization with SkySat imagery aids in ICESat-2 surface height evaluation, and thus ICESat-2 surface heights can be utilized to characterize crevasse types.

# 6. Applications to crevasse detection and characterization of Jakobshavn Isbræ

# 6.1. Objective: height measurement, validation and characterization of crevasse morphologies for Jakobshavn Isbræ

In this section, we take the topic of surface height determination and crevasse characterization a step further: The objective is to demonstrate that ICESat-2 measurements can be employed to differentiate between different types of fast-moving ice – surging and fast-moving glaciers – and that the DDA-ice can retain characteristics of crevasse morphology indicative of different acceleration types. To this end, we analyze ATLAS data from Jakobshavn Isbræ, Greenland (see, Table 4) and validate our findings using high-resolution image data from Planet SkySat, which were specifically collected for this purpose (see, Fig. 7).

As described in (Mayer and Herzfeld, 2000), a surging glacier has characteristically different crevasse patterns than a continuously fast-moving ice stream. Jakobshavn Isbræ is used as the prototype of a continuously fast-moving and accelerating glacier. In order to compare the crevasse characteristics of the surging Negribreen to those of the continuously fast-moving Jakobshavn Isbræ, we summarize a few distinctive properties of Jakobshavn Isbræ. The ice stream follows a subglacial trough, which is the cause of the spatial acceleration from the

slow motion of the Greenland Ice Sheet to the continuously fast flow of the ice stream (Mayer and Herzfeld, 2000; Herzfeld et al., 2014b). The continued action of the deformation processes associated with the fast flow leads to a prevalence of several types of closed conjugate shear crevasses in the center of the ice stream. Despite significant additional acceleration and surface-lowering during the observation time of ICESat (2003–2009), the same crevasse provinces persisted through at least 2009, a result derived in (Herzfeld et al., 2014b) based on surface-roughness analysis of ASTER imagery (15 m resolution in panchromatic channel), ICESat GLAS data and Airborne Topographic Mapper (ATM) data (Krabill et al., 1995). Data from Jakobshavn Isbræ are included to investigate the potential of deriving more detailed information from image and altimeter data sets of higher resolution (0.7 m)

## 6.2. Comparative analysis of ICESat-2 ATLAS data and SkySat data

Planet SkySat imagery was collected over Jakobshavn Isbræ in four passes on four days between 2019-Oct-20 and 2019-Oct-26 (see, Fig. 8 for spatial coverage of the SkySat stripes). An exemplary result of the visualization tool, introduced in Section 5.1, is shown in Fig. 8, which renders a synoptical comparison of a SkySat image from 2019-Oct-24 (ssc1 data, 0.86 m pixel size) and ICESat-2 data from RGT 666 collected on 2019-May-11 (track gt3l). A comparative analysis across six months of time separation is meaningful because of the above-mentioned stability of the structural provinces of Jakobshavn Isbræ. Fig. 8a shows a multi-generational crevasse type characteristic of the center of the ice

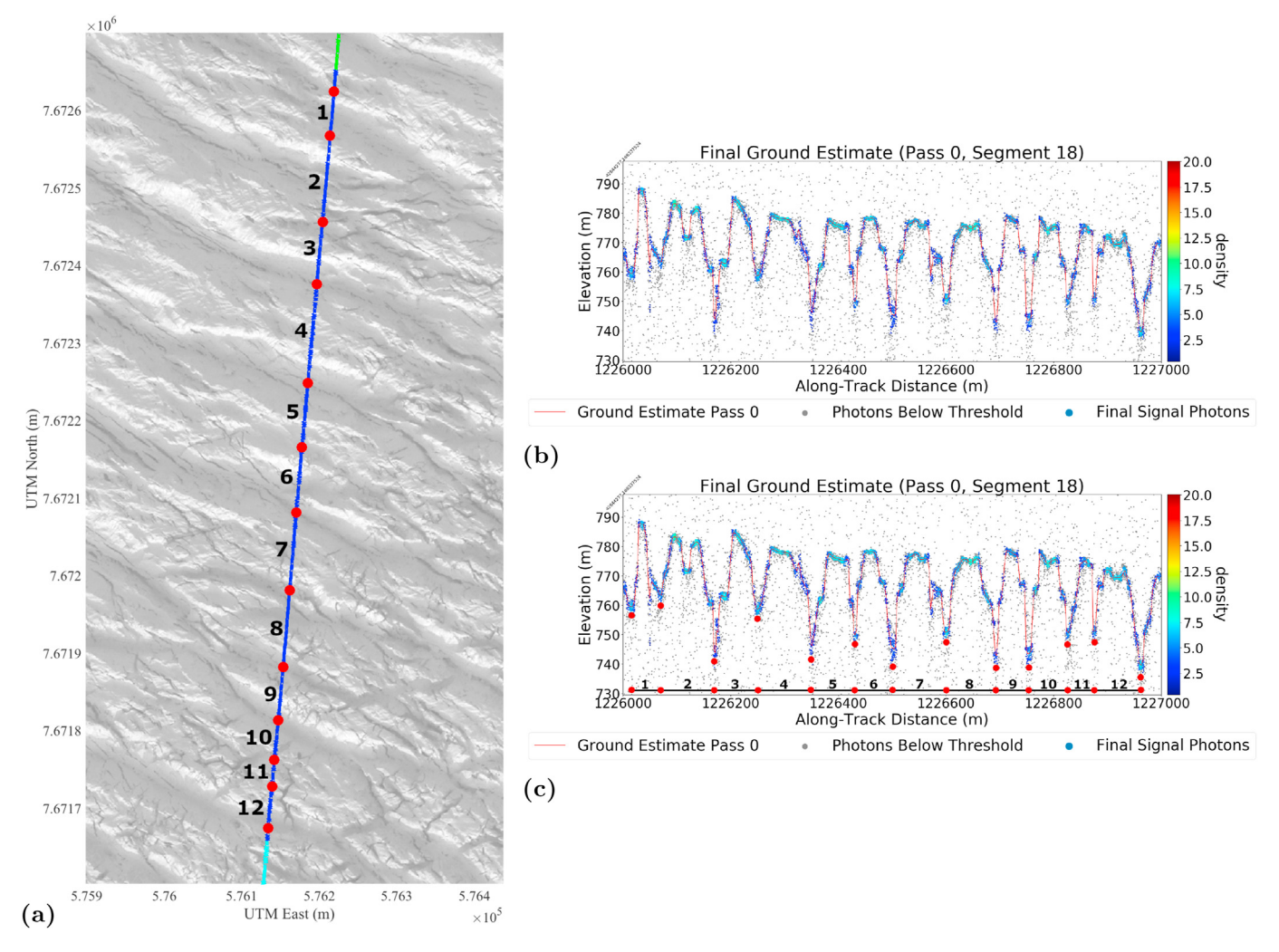


Fig. 8. Comparison of SkySat image of complexly crevassed region in Jakobshavn Isbræ (Ilulissat Ice Stream, South Ice Stream) with DDA-ice surface heights from ICESat-2. [Planet SkySat Image: 20191024\_151720\_ssc1\_u0003\_pansharpened\_dn.tif], [ICESat-2 ATLAS granule: ATL03\_20190511210825\_06660305\_002\_02.h5] [RGT 666 gt3l (strong beam), collected 2019-May-11 at 21:08 GMT = 19:08 local time, day-time data]. (a) SkySat Image with ICESat-2 track superimposed. ICESat-2 track is approximately normal to flow direction (see Fig. 8). Descending track. SkySat ssc1 data have 0.86 m pixel size. (b) DDA-ice surface-height determination from ICESat-2 data. Left side of surface-height plot is North (top) in SkySat image (b). (c) Same as (b), with red dots identifying individual crevasses matching dots in SkySat image (b). Despite 6 month separation of observation time between SkySat and ICESat-2, average crevasse spacing is 81.37 m (DDA-ice ICESat-2 altimetry) and 81.25 m (SkySat Imagery). For individual crevasse spacings, see Table 5. (For interpretation of the references to color in this figure legend, the reader is referred to the Web version of this article.)

stream in imagery, and the right panel provides the result of the DDA-ice applied to ICESat-2 data (the top of the SkySat image corresponds to the left in the ICESat-2 segment). Co-geolocation is not perfect, but it is possible to identify each individual crevasse and its sub-features (shoulders and bottoms) in both the SkySat image (Fig. 8a) and the ATLAS surface height profile (Fig. 8b), as indicated in Fig. 8c. The time difference adds of course to lack of co-geolocation, as the ice moves, while the structural provinces remain the same. ATLAS surface heights are rendered with 2.5-m ground-follower intervals.

To substantiate the comparison, we conduct a mathematical and a morphological analysis of crevasse characteristics in SkySat imagery and ICESat-2 DDA-ice results.

## Mathematical analysis

Crevasses with at least 20 m depth, as determined by the DDA-ice results, are marked with red dots in Fig. 8c. The corresponding crevasses are identified in the SkySat image (red dots in Fig. 8a). Crevasse spacing estimates from the two data sources, given in Table 5, are remarkably similar: 81.37 m from the DDA-ice and 81.25 m from the SkySat image. Individual crevasse spacings, labeled by black numbers in

Fig. 8a and c, also correspond well differing by an average of 0.12 m  $\pm$  11.6 m across the 12 segments. Most of the differences in individual spacing are attributed to the 5 month difference between ATLAS and SkySat acquisition dates.

## Morphological analysis

There is an amazingly accurate agreement between the laser altimeter profiles from ICESat-2, resultant from analysis with the DDA-ice, and imagery from SkySat. The agreement is better than that of individual crevasses – smaller features such as shoulders inside a crevasse and thin deeper openings can be identified, and each single crevasse crossing can be matched between the two instruments. The fact that subordinate, thin and deep crevasses are visible in the SkySat image indicates that these types of features exist in reality. In conclusion, the ATLAS instrument has the ability to penetrate into very thin crevasses at the bottom of crevasse groups. Stated as an algorithm property, the DDA-ice identifies narrow and deep extensions from the bottom of older crevasses, which increase depth by an additional 15–30 m; these are not artifacts of the algorithm, as the SkySat imagery shows. The DDA-ice measures depths to 45 m, with an average of 35–40 m, and resolves crevasse morphology. This

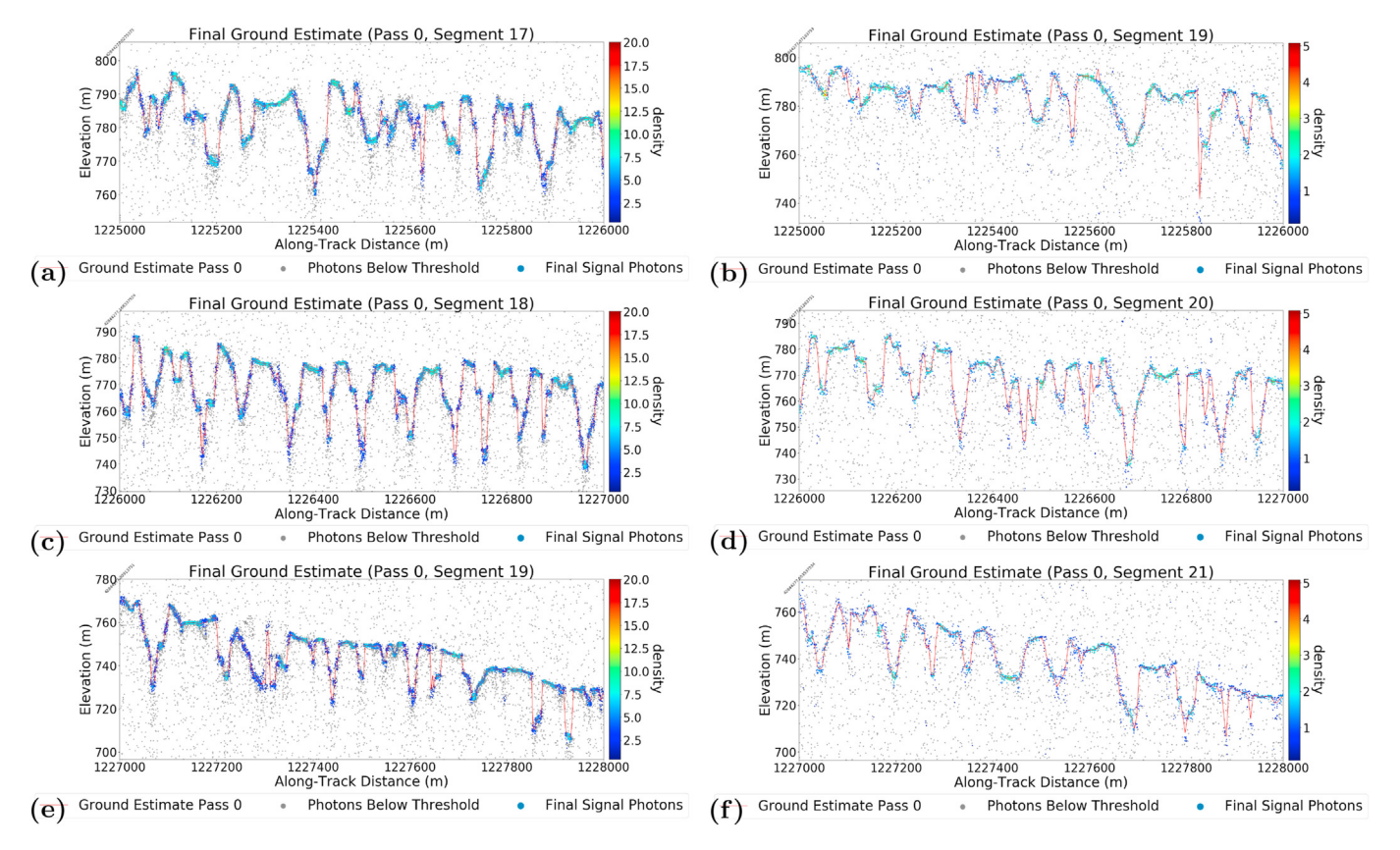


Fig. 9. Surface-height determination resultant from DDA-ice algorithm for crevassed regions in Jakobshavn Isbræ (Ilulissat Ice Stream, South Ice Stream). [ATL03\_20190511210825\_06660305\_002\_02. h5] [RGT 666 gt3l (strong beam) [left column] and gt3r (weak beam) [right column], collected 2019-May-11 at 21:08 GMT = 19:08 local time, day-time data]. ICESat-2 track is approximately normal to flow direction of Jakobshavn Isbræ, see Fig. 8.

agreement between imagery and altimetry also demonstrates that the DDA-ice has the ability to automatically identify surface heights across very complex surface structures, with an auto-adaptive algorithm. The algorithm parameters work across surfaces of very different patterns and features.

## 6.3. Comparison of weak and strong beam data for Jakobshavn Isbræ

A comparative analysis of results from weak-beam analysis with those of strong-beam analysis for Jakobshavn Isbræ (Fig. 10) confirms the results already obtained in Section 4 for Negribreen data. Fig. 10 shows surface heights for three segments of profiles with different crevasse characteristics. Both the weak and the strong beam signal photon data sets and ground followers reveal the complex characteristics of the crevasse types in the center of the ice stream: For segment 18, crevasse groups with deeper crevasse extensions are seen in both types of beams. In segment 17, wide open crevasses interchange with narrow, complex crevasses, and for segment 19 a section of regularly-spaced crevasses is observed among wide open and irregularly spaced crevasses. Recalling that along-track offset between weak and strong beams in a pair is 2.5 km and across-track difference is 90 m, we conclude that ATLAS data from the weak beam can also be utilized to characterize ice-surface morphology and crevasse types (when analyzed with the DDA-ice).

## 6.4. Comparison to Negribreen

In general, recent surge crevasses (as found in RGT 594) are characterized by regular shapes (due to a single opening event), more regular spacing (also a single event), and sharp edges. Crevasse edges round off, due to the repeated effects of snow fall, melting, wind erosion and redeposition. The roundedness of crevasses allows for relative dating of crevasse openings (Herzfeld et al., 2013). Crevasse types in the

Jakobshavn region are generally multi-generational and multi-directional types, due to the fact that the ice has experienced several different deformational forces while moving downglacier. The continuously fast movement leads to repeated actions of mostly complex and conjugate shear deformations.

# 7. Comparison of DDA-ice capabilities with ATL03 signal classification and ATL06 ice-surface-height determination

The objective of this section is to compare the capabilities of the DDA-ice with the results reported in NASA ICESat-2 standard products, ATL03 and ATL06 (Neumann et al., 2019c; Smith et al., 2019c). The DDA-ice performs data aggregation, signal identification (also termed signal classification, i.e. separation of signal and noise, or signal and background), determination of discrete surface height including height inside crevasses, and estimation of surface height in every along-track location by a ground follower. In the ICESat-2 standard products, signal classification is carried out as an attribute of the Global Geolocated Photons, reported in ATL03 (Neumann et al., 2019b), while ice-surface-height determination is performed for the Land Ice Along-Track Height Product, ATL06 (Smith et al., 2019a).

The signal-finding algorithm used in ATL03 is described in (Neumann et al., 2019b), i.e. the ATBD matching the data release version r002, which are the data analyzed in this paper. In (Neumann et al., 2019b), reference is given to a companion document that describes "Optimization of Signal Finding Algorithm" (Neumann et al., 2019b) (p. 54). The ATL03-signal finding algorithm builds on an algorithm developed by Anita Brenner (pers. comm., 2013). In a nutshell, the ATL03-signal finding algorithm is a histogram-based algorithm (histograms of photon counts in along-track intervals are analyzed). Other than the DDA-ice, the ATL03 signal finding algorithm distinguishes many hard-coded cases, which depend on surface slope, background-photon

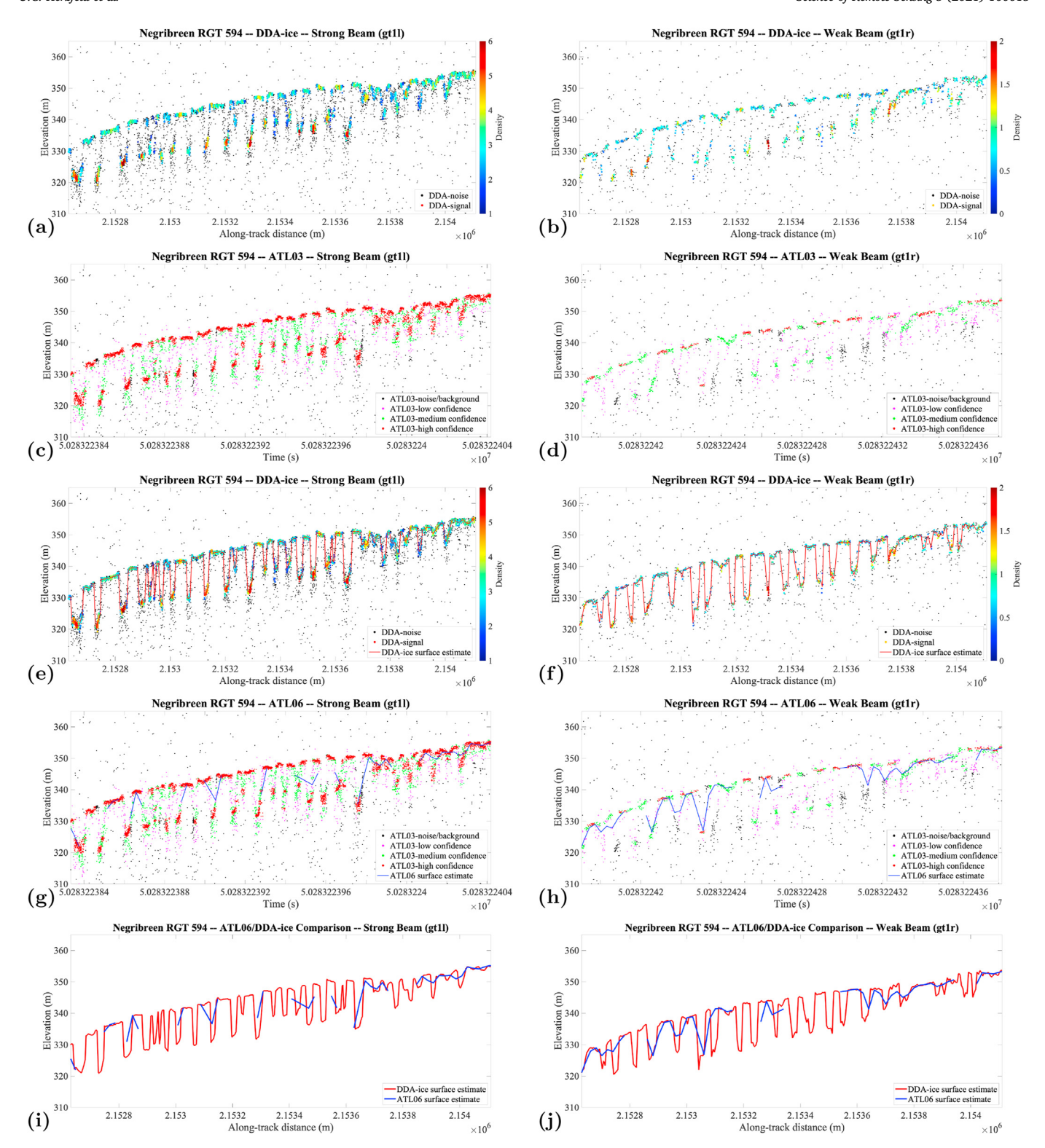


Fig. 10. Comparison of results from DDA-ice algorithm with ATL03 signal classification/ATL06 surface height determination. Negribreen RGT594, night-time data, simple crevassing. [ATL03\_20190805232841\_05940403\_002\_01. h5] [RGT 594 gt1l, strong beam [left column] and RGT 594 gt1r, weak beam [right column], collected 2019-Aug-05, 23:28 GMT = 1:28 local time, night-time/low twilight data]. ATL06 surface heights from [ATL06\_20190805232841\_05940403\_002\_01.h5]. (a), (b) DDA-ice photon classification with density values. For description, see Fig. 4. (c), (d) ATL03 signal classification. (e), (f) DDA-ice surface-height determination with auto-adaptive ground follower based on density field in (a), (b). (g), (h) ATL06 surface-height determination based on ATL03 signal classification in (c), (d). (i), (j) Comparison of DDA-ice surface determination wit ATL06 surface determination.

rate, and includes steps such as outlier removal and signal padding. Prior to the main signal-finding steps, the ATL03 algorithm builds on analysis of atmospheric histograms and relies on pre-determined regions for surface types (land, ocean, sea ice, land ice and inland water). The ATL03 signal finder returns three classes of signals, labeled high, medium and low confidence signals, and noise/background.

In contrast, the DDA-ice does not classify by signal confidence, but instead utilizes the density field in several respects. Density of a single photon can be viewed as an absolute, but also as a relative measure of the significance of a returned signal photon, which allows for the auto-adaptive capability of the algorithm.

The determination of ice-surface height is described in ATL06 (Smith et al., 2019a), which utilizes the ATL03 signal determination. The resultant ATL06 surface heights are averages derived from 40-m segments, posted every 20-m along-track. Discrete surface heights from the DDA-ice are posted for each signal photon, i.e. at the sensor resolution of nominally 0.7 m. Interpolated surface heights are derived at 2.5 m or 5 m, depending on surface roughness, for the strong beams and at 5 m everywhere for the weak beams.

In our comparison, we distinguish the following cases: (a) night-time data (low density of background photons) and day-time data (higher density of background photons), (b) ICESat-2 ATLAS strong and weak beams (where transmit energy of strong beams is four times that of weak beams), and (c) simple and complex crevasse morphologies. The mathematically easier detection cases are (a) night-time data, (b) strong-beam data, and (c) simple crevasse morphologies, the more challenging ones are (a) day-time data, (b) weak-beam data, and (c) complex morphologies, other combinations fall in between. A segment of Negribreen data from RGT594 is used as the example for night-time/low-twilight data (collected at 1:28am in August at 78° Northern latitude), this segment includes data segments analyzed in Section 4, but is longer (1.5 km) to include different crevasse morphologies (simple and more complex ones) (Fig. 10). A segment of Jakobshavn Isbræ data from RGT666 is employed to investigate the situation for day-time data (collected at 19:08 local time in May at 69° Northern latitude), this segment is about 3 km long and includes some of the data analyzed in Section 6, which represent complex crevasse morphologies.

## 7.1. Negribreen, night-time data, simple crevassing (Fig. 10)

Fig. 10 shows that in a situation where surfaces between crevasses as well as crevasse bottoms constitute the strongest return and background is low (night-time data), the ATL03 signal finder correctly identifies those photons in the high-confidence class (Fig. 10b, left two thirds of figure panel). In some locations, medium-likelihood photons are those reflected from the crevasse walls. However, in locations where the surface is a bit more complex (Fig. 10b, right third of panel), the classifier is not able to separate surface and crevasse bottoms. Photons labeled as low-confidence signal photons include many false positives. This evaluation is based on visual comparison with the DDA-ice signal photon field in Fig. 10a.

However, most glaciologists will use ice-surface heights from ATL06, rather than the photon cloud, in their analysis, and this result is given in Fig. 10g as ATL06 heights superimposed on the ATL03 photon classification. Clearly, the ATL06 surface-height-determination algorithm generally fails over crevassed surfaces, even for the mathematically easiest case of low-background, night-time data and a simple crevasse morphology.

Fig. 10e shows that the DDA-ice ground follower, based on the density field and signal classification given in Fig. 10a, correctly identifies surface heights in all crevasse types (in this example) and automatically adapts to the change in morphology at two thirds of the along-track distance in the figure panel. The increased information content afforded by the DDA-ice, compared to the ATL06 data product, is obvious from Fig. 10i. In conclusion, the information included in the density-dimension is salient for surface-height determination in crevassed

terrain, for strong-beam and weak-beam data.

The situation is worse for weak-beam data, as seen in Fig. 10 (right column). In this case, the ATL03 signal classifier correctly assigns about half of the surface reflections to the class of high-confidence signal photons, while the other half of surface reflections falls in the medium-confidence class and crevasse bottoms are classified as medium-confidence signal or noise photons (Fig. 10d). The DDA-ice correctly identifies surface and crevasse reflections as signal photons (Fig. 10b). The ATL06 surface determination generally fails in this case as well (Fig. 10h,j), whereas the DDA-ice yields a result that retrieves surface heights from weak-beam data (Fig. 10f).

# 7.2. Jakobshavn Isbræ, day-time data, complex crevasse morphology (Fig. 11)

As seen in Section 5, the situation is more complex for the example from Jakobshavn Isrbæ, both with regard to signal-to-background ratios and complexity of crevasse shapes. The DDA-ice results in correctly retrieved signal photons and surface following that shows the complex crevasse morphology, for both the strong-beam and the weak-beam data (Fig. 11a,b,e,f). The ATL03 signal finder performs significantly worse than for night-time data. In this case, ice surface segments between crevasses are only partly assigned to the high-confidence class and about half to the medium-confidence class, already for the strong-beam data (Fig. 10c). On a positive note, many reflections from crevasses are included in the low-confidence signal class, for the strong beam data. For the case of the weak beam, no high-confidence signal photons are found in the entire segment (Fig. 10d), and surface as well as crevasse returns are classified as low-confidence signal or noise photons. Again, the ATL06 surface finder generally fails for both the strong-beam data and the weak-beam data (Fig. 10g and h) and the information gain from the DDA-ice is compelling (Fig. 10i and j).

In summary, the DDA-ice measures crevasses, with a surface that follows height into and out of crevasses, whereas surface heights in crevassed terrain are generally not resolved in ATL06. The examples given here are typical for crevassed and otherwise complex surfaces. The striking information gain is attributed to the fact that the DDA-ice is designed to match the properties of the photon-counting laser altimeter system and the resultant data sets.

The DDA-ice is not only an efficient algorithm for ice-surface-height determination, it is also mathematically more simple and aesthetical, as it provides a mathematically closed solution to the problems of signal classification and surface-height determination. The key characteristics that lead to the algorithm's overall performance are that the DDA-ice is auto-adaptive at several steps of the algorithm and that each step utilizes the additional "dimension" of density. The algorithm also automatically adapts to surface roughness.

## 8. Summary and conclusions

This paper highlights the revolutionary capability of ICESat-2 ATLAS data to retrieve surface heights of heavily crevassed, rapidly accelerating glaciers from micro-pulse photon-counting laser altimeter data. This capability is afforded by the introduction of an innovative algorithm for surface-height determination, the density-dimension algorithm for ice surfaces (DDA-ice). The DDA-ice allows a fascinating retrieval of crevasse shapes and types in many details of the height profile. In consequence, crevasse types of surging and other types of fast-moving glaciers can be discriminated using morphological characteristics captured in the altimetry retrievals. Using DDA-ice analysis, ICESat-2 data open the path for a novel approach to analysis of different types of fast-moving and accelerating glaciers based on surface signatures of ice dynamics.

The DDA-ice provides an alternative to the standard processing algorithm applied to derive the ICESat-2 standard land-ice along-track height product, ATL06, which reduces the 0.7-m spaced along-track altimeter data to 40-m along-track average heights with 20-m spaced

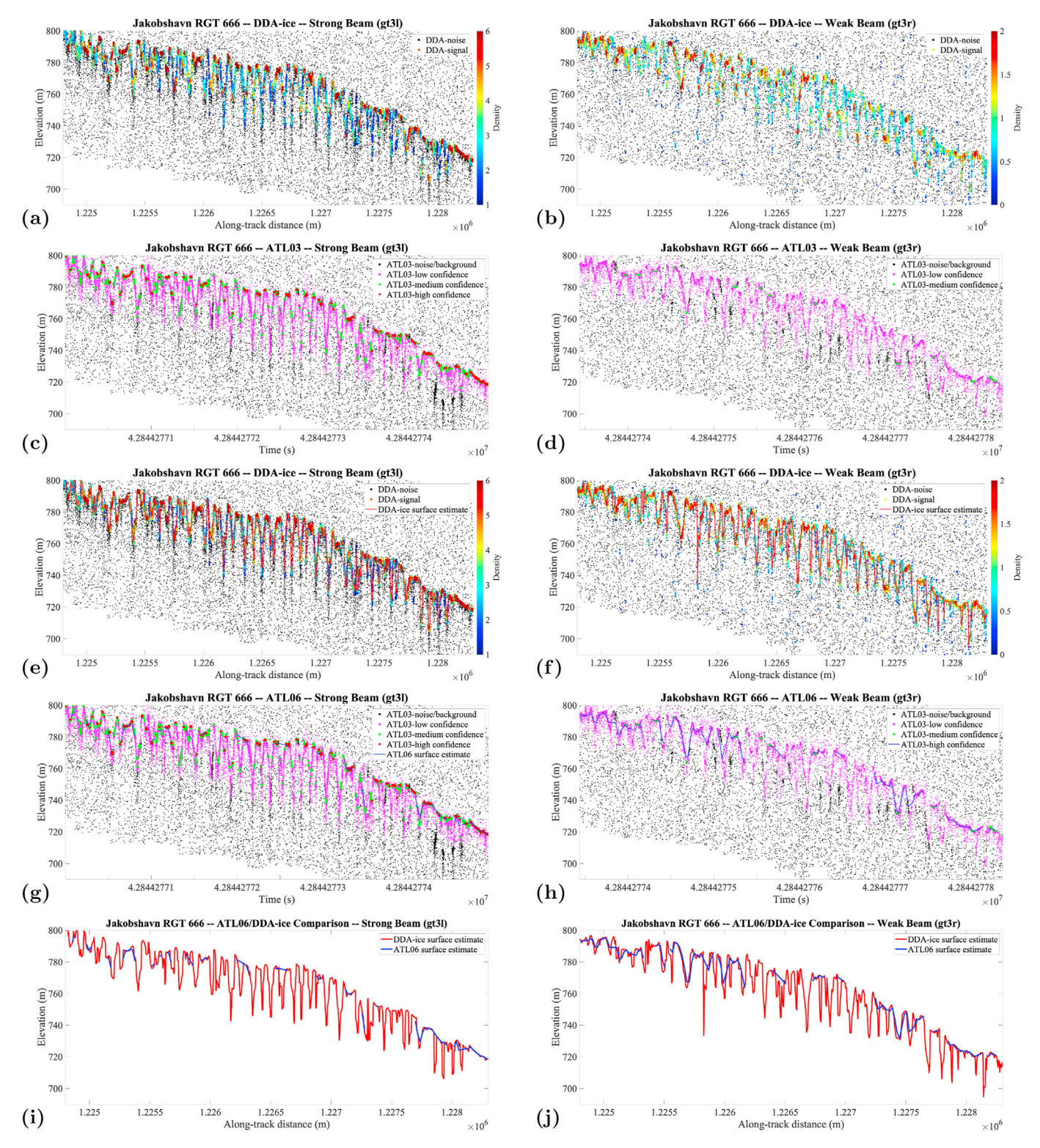


Fig. 11. Comparison of results from DDA-ice algorithm with ATL03 signal classification/ATL06 surface height determination. Jakobshavn Isbræ RGT666, day-time data, complex crevassing. See also Figs. 8–10. [ATL03\_20190511210825\_06660305\_002\_02.h5] [RGT 666 gt3l, strong beam [left column] and RGT [RGT 666 gt3r, weak beam [right column], collected 2019-May-11 at 21:08 GMT = 19:08 local time, day-time data]. ATL06 surface heights from [ATL06\_20190511210825\_06660305\_002\_01.h5]. (a), (b) DDA-ice photon classification with density values. For description, see Fig. 4. (c), (d) ATL03 signal classification. (e), (f) DDA-ice surface-height determination with auto-adaptive ground follower based on density field in (a), (b). (g), (h) ATL06 surface-height determination based on ATL03 signal classification in (c), (d). (i), (j) Comparison of DDA-ice surface determination wit ATL06 surface determination.

posting and often fails over crevassed surfaces. The DDA-ice provides a mathematically closed solution to signal-background classification and surface-height determination for data from both the strong and weak ATLAS beams, with a signal finder that consistently identifies photons from complex reflectors under variable background characteristics. Thus it constitutes a significant advance over the ATLO3 signal classifier, which in essence fails to yield a consistent photon classification in complex situations, in both strong and weak beams, with variable severity of misclassification depending on the type of surface morphologies and background characteristics. Conceptually, the compelling information gain of the DDA-ice results compared to signal finding in ATLO3 and surface-height determination in ATLO6 is explained by the design of the DDA-ice as an algorithm that matches the properties of the photon-counting laser altimeter system and the resultant data sets.

In this paper, we have (1) introduced the Density-Dimension Algorithm for ice surfaces, the DDA-ice, and demonstrate its functionality for surface-height determination from ICESat-2 ATLAS data over crevassed ice surfaces, but also for simple, uncrevassed ice surfaces, (2) validated the approach using airborne geophysical data collected over the surging Negribreen, an active surge glacier in Arctic Svalbard, and (3) compared ICESat-2 data to modern high-resolution (0.72 m or 0.86 m) image data from Planet SkySat, specifically acquired with ICESat-2 measurement and algorithm evaluation in mind.

Specific results include the following: (1) Crevasse characteristics, including mean and maximal depth and average spacing of crevasses, from ICESat-2 data match those derived from airborne altimeter data. (2) Surface heights and surface morphological characteristics can be retrieved from the strong beams and also from the weak beams, which have one-fourth of the transmit energy of the strong beams. (3) The DDAice allows identification of crevasse shapes and types from details of a complex height profile, as substantiated through comparison of ICESat-2 surface heights with SkySat image data from Jakobshavn Isbræ. Crevasse depths of up to 45 m are generally measured. (4) Comparison of surface and crevasse morphological characteristics in ICESat-2 data from the surging Negribreen and the continuously fast-moving and accelerating Jakobshavn Isbræ (Ilulissat Ice Stream), Greenland, indicates that classification of dynamic types will be feasible based on the DDA-ice analyzed ICESat-2 data. The sudden acceleration of a surge results in freshly-opened, clear-cut crevasses, which are characterized by sharp edges, as observed for Negribreen. In contrast, the continued action of crevasse formation, transport and closure that acts on the ice in a continuously fast-moving glacier results in several types of closed conjugate shear crevasses with eroded edges, due to ablation, melting, snowfall and wind, and repeated crevasse patterns. (5) Geostatistical characterization of surface roughness, calculated from ICESat-2 DDA-ice results and airborne altimeter data, serves to further evaluate the ICESat-2 results. Comparison with crevasse provinces captured in SkySat data over Negribreen indicates that ICESat-2 surface heights can be utilized to characterize crevasse classes and provides a context to surge dynamics.

## Data availability

Landsat-8 products are available from the U.S. Geological Survey (USGS) Earth Resources Observation and Science (EROS) Center, see htt ps://www.usgs.gov/centers/eros/data-tools and https://glovis.usgs.gov/. Sentinel data were collected by the European Space Agency (ESA) as part of the Copernicus Missions and can be downloaded via https://scihub.copernicus.eu/.

## **Author contributions**

UCH designed the study, carried out part of the analysis and wrote the paper. TT carried out part of the analysis and contributed to writing the paper. ML, JH and GM contributed to data analysis and writing the paper.

### **Declaration of competing interest**

The authors declare that they have no known competing financial interests or personal relationships that could have appeared to influence the work reported in this paper.

#### Acknowledgements

Thanks are due to our pilot and technician, Harald Sandal and Gustav Svanström, Airlift, Norway, of the 2019 Negribreen campaign, to Jack Kohler, Geir Ove Aspnes, Jørn Dybdahl, Norwegian Polar Institute, and Chris Borstad, University Center in Svalbard (UNIS), now University of Montana, to Inger Jennings (SIOS) and Kristin Woxholth, Longyearbyen, for help with logistical support, to the ICESat-2 Project, especially Thomas Neumann, Kaitlin Harbeck, David Hancock and Anthony Martino for collaboration and support regarding ICESat-2, to Compton Tucker and Manil Maskey (NASA) and Paris Good, Planet, for coordination of SkySat data acquisition, and to Tasha Markley, Alfredo de la Pena Gonzalez and Henry Cobb, Geomathematics Group, University of Colorado Boulder, for assistance with data analysis. We also like to thank two anonymous reviewers for the suggestions to include a detailed comparison of DDA-ice capabilities with results from ICESat-2 products ATL03 ad ATL06 results and other notes which generally helped to improve the paper. Research and data collection were supported by the U.S. National Aeronautics and Space Administration (NASA) Earth Sciences Division under awards 80NSSC20K0975, 80NSSC18K1439 and NNX17AG75G and by the U.S. National Science Foundation (NSF) under awards OPP-1745705 and OPP-1942356 (Principal Investigator for all awards: Ute Herzfeld). The helicopter was provided by the Norwegian Polar Institute and operated by Airlift. Collection of airborne data was conducted with permission of the National Security Authority of Norway, the Civil Aviation Authority of Norway and the Governor of Svalbard, registered as Research in Svalbard Project RIS-10827 "NEGRIBREEN SURGE". The data collection was also partly supported through a 2018 Access Pilot Project (2017\_0010) of the Svalbard Integrated Observing System (SIOS). All this support is gratefully acknowledged.

## Appendix A. Supplementary data

Supplementary data to this article can be found online at https://doi. org/10.1016/j.srs.2020.100013.

### References

- Abdalati, W., Zwally, H.J., Bindschadler, R., Csatho, B., Farrell, S., Fricker, H., Harding, D., Kwok, R., Lefsky, M., Markus, T., et al., 2010. The ICESat-2 laser altimetry mission. Proc. IEEE 98 (5), 735–751.
- Bindschadler, R., Nowicki, S., Abe-ouchi, A., Aschwanden, A., Choi, H., Fastook, J., Granzow, G., Gutowski, G., Herzfeld, U., Jackson, C., Johnson, J., Khroulev, C., Levermann, A., Lipscomb, W.H., Martin, M.A., Morlighem, M., Parizek, B., Pollard, D., Price, S., Ren, D., Saito, F., Sato, T., Seddik, H., Seroussi, H., Takahashi, K., Walker, R., Wang, W.L., 2013. Ice-sheet model sensitivities to environmental forcing and their use in projecting future sea-level (the SeaRISE project). J. Glaciol. 59 (214).
- Crocker, R.I., Maslanik, J.A., Palo, S.E., Adler, J.J., Herzfeld, U.C., Emery, W.J., 2011.
  A sensor package for ice surface characterization using small unmanned aircraft systems. IEEE Trans. Geosci. Rem. Sens. 49 (99), 1–15.
- Dabney, P.W., Harding, D.J., Abshire, J., Huss, T., Jodor, G., Machan, R., Marzouk, J., Rush, K., Seas, A., Shuman, C., Others, 2010. The slope imaging multi-polarization photon-counting lidar: development and performance results. In: Geoscience and Remote Sensing Symposium (IGARSS), 2010 IEEE International. IEEE, pp. 653–656.
- Davis, C.H., 1992. Satellite radar altimetry. microwave theory and techniques. IEEE Transactions on 40 (6), 1070–1076.
- Davis, A.B., Marshak, A., 2004. Photon propagation in heterogeneous optical media with spatial correlations: enhanced mean-free-paths and wider-than-exponential free-path distributions. J. Quant. Spectrosc. Radiat. Transf. 84 (1), 3–34.
- Hall, D.K., Comiso, J.C., DiGirolamo, N.E., Shuman, C.A., Box, J.E., Koenig, L.S., 2013.
  Variability in the surface temperature and melt extent of the Greenland ice sheet from modis. Geophys. Res. Lett. 40 (10), 2114–2120.
- Harding, D.J., Dabney, P.W., Valett, S., 2011. Polarimetric, two-color, photon-counting laser altimeter measurements of forest canopy structure. In: International Symposium

- on Lidar and Radar Mapping Technologies. International Society for Optics and Photonics, 828629.
- Herzfeld, U.C., 2008. Master of the obscure automated geostatistical classification in presence of complex geophysical processes. Math. Geosci. 40 (5), 587–618.
- Herzfeld, U.C., Mayer, H., 1997. Surge of Bering Glacier and Bagley Ice Field, Alaska: an update to August 1995 and an interpretation of brittle-deformation patterns. J. Glaciol. 43 (145), 427–434.
- Herzfeld, U.C., Clarke, G.K.C., Mayer, H., Greve, R., 2004. Derivation of deformation characteristics in fast-moving glaciers. Comput. Geosci. 30 (3), 291–302.
- Herzfeld, U., Fastook, J., Greve, R., McDonald, B., Wallin, B., Chen, P., 2012. On the influence of Greenland outlet glacier bed topography on results from dynamic ice sheet models. Ann. Glaciol. 53 (60), 281–293.
- Herzfeld, U.C., McDonald, B., Stachura, M., Hale, R.G., Chen, P., Trantow, T., 2013. Bering Glacier surge 2011: analysis of laser altimeter data. Ann. Glaciol. 54 (63), 158–170.
- Herzfeld, U., McDonald, B., Wallin, B., Markus, T., Neumann, T., Brenner, A., 2014a. An algorithm for detection of ground and canopy cover in micropulse photon-counting lidar altimeter data in preparation of the ICESat-2 mission. IEEE Trans. Geosci. Rem. Sens. 54 (4), 2109–2125.
- Herzfeld, U.C., McDonald, B., Wallin, B.F., Krabill, W., Manizade, S., Sonntag, J., Mayer, H., Yearsley, W.A., Chen, P.A., Alexander, W., 2014b. Elevation changes and dynamic provinces of Jakobshavn Isbræ, Greenland, derived using generalized spatial surface roughness from ICESat GLAS and ATM data. J. Glaciol. 60 (223), 834–848.
- Herzfeld, U.C., Trantow, T., Harding, D., Dabney, P.W., 2017. Surface-height determination of crevassed glaciers — mathematical principles of an Auto-Adaptive Density-Dimension Algorithm and validation using ICESat-2 Simulator (SIMPL) data. IEEE Trans. Geosci. Rem. Sens. 55 (4), 1874–1896.
- Herzfeld, U.C., Palm, S., Hancock, D., 2020. ICESat-2 Algorithm Theoretical Basis Document for the Atmosphere, Part II: Detection of Atmospheric Layers and Surface Using a Density Dimension Algorithm, v11.0, February 6, 2020. NASA ICESat-2 Project, 374pp.
- Krabill, W., Thomas, R., Martin, C., Swift, R., Frederick, E., 1995. Accuracy of airborne laser altimetry over the Greenland Ice Sheet. Int. J. Rem. Sens. 16, 1211–1222.
- Lefauconnier, B., Hagen, J.O., 1991. Surging and Calving Glaciers in Eastern Svalbard. Norsk Polarinstitutt.
- Luthcke, S.B., Pennington, T., Rebold, T., Taylor, T., 2019. Algorithm Theoretical Basis Document (ATBD) for ATL03g ICESat-2 Receive Photon Geolocation, October, 28th, 2019. NASA ICESat-2 Project, 63pp.
- Luthcke, S.B., Rowlands, D.D., McCarthy, J.J., Pavlis, D.E., Stoneking, E., 2000.
  Spaceborne laser-altimeter-pointing bias calibration from range residual analysis.
  J. Spacecraft Rockets 37 (3), 374–384.
- Luthcke, S.B., Carabajal, C.C., Rowlands, D.D., 2002. Enhanced geolocation of spaceborne laser altimeter surface returns: parameter calibration from the simultaneous reduction of altimeter range and navigation tracking data. J. Geodyn. 34 (3–4), 447–475.
- Luthcke, S.B., Zelensky, N.P., Rowlands, D.D., Lemoine, F.G., Williams, T.A., 2003. The 1-centimeter orbit: JASON-1 precision orbit determination using GGPS, SLR, DORIS, and altimeter data special issue: JASON-1 calibration/validation. Mar. Geodes. 26 (3–4). 399–421.
- Luthcke, S.B., Rowlands, D.D., Williams, T.A., Sirota, M., 2005. Reduction of ICESat systematic geolocation errors and the impact on ice sheet elevation change detection. Geophys. Res. Lett. 32 (21).
- Markus, T., Neumann, T., Martino, A., Abdalati, W., Brunt, K., Csatho, B., Farrell, S.d, Fricker, H., Gardner, A., Harding, D., et al., 2017. The Ice, Cloud, and land Elevation Satellite-2 (ICESat-2): science requirements, concept, and implementation. Rem. Sens. Environ. 190, 260–273.
- Marshak, A., Davis, A., 2005. 3D Radiative Transfer in Cloudy Atmospheres. Springer Science & Business Media.
- Martino, A.J., Bock, M.R., Gosmeyer, C., Field, C., Neumann, T.A., Hancock, D.W., Jones, R.L., Dabney, P.W., Webb, C.E., Lee, J., 2019. CLOUD, and Land Elevation Satellite (ICESat-2) Project: Algorithm Theoretical Basis Document (ATBD) for ATL02 (Level 1B) Data Product Processing, July 29th, 2019. NASA ICESat-2 Project, 107pp.
- Mayer, H., Herzfeld, U.C., 2000. Structural glaciology of the fast-moving Jakobshavn Isbræ, Greenland, compared to the surging bering glacier, Alaska, USA. Ann. Glaciol. 30 (1), 243–249.
- Medley, G., 2016. Detection and Characterization of Ice Surface Elevation Profiles from Micropulse Photon-Counting LiDAR Data. Master's thesis. Master Thesis in Applied Mathematics, University of Colorado Boulder.
- Miller, L.S., Hayne, G.S., 1972. Characteristics of Ocean-Reflected Short Radar Pulses with Application to Altimetry and Surface Roughness Determination, 1. NOAA Sea Surface Topography from Space.

- Neumann, T.A., Martino, A.J., Markus, T., Bae, S., Bock, M.R., Brenner, A.C., Brunt, K.M., Cavanaugh, J., Fernandes, S.T., Hancock, D.W., 2019a. The ice, cloud, and land elevation satellite–2 mission: a global geolocated photon product derived from the advanced topographic laser altimeter system. Rem. Sens. Environ. 233, 111325.
- Neumann, T., Brenner, A., Hancock, D., Robbins, J., Jack, S., Harbeck, K., Gibbons, A., Lee, J., Scott, L., Rebold, R., 2019b. ICESat-2 Algorithm Theoretical Basis Document for Global Geolocated Photons, October 15, 2019. NASA ICESat-2 Project, 202pp.
- Neumann, T., Brenner, A., Hancock, D., Scott, L., Lee, J., Robbins, J., Harbeck, K., Saba, J., Brunt, K., Gibbons, A., 2019c. ATLAS/ICESat-2 L2A Global Geolocated Photon Data, Version 2. Boulder, Colorado USA.
- Nghiem, S.V., Hall, D.K., Mote, T.L., Tedesco, Marco, Albert, M.R., Keegan, K., Shuman, C.A., DiGirolamo, N.E., Neumann, G., 2012. The extreme melt across the Greenland Ice Sheet in 2012. Geophys. Res. Lett. 39 (20).
- Nowicki, S., Bindschadler, R., Abe-ouchi, A., Aschwanden, A., Choi, H., Fastook, J., Granzow, G., Gutowski, G., Herzfeld, U., Jackson, C., Johnson, J., Khroulev, C., Levermann, A., Lipscomb, W.H., Martin, M.A., Morlighem, M., Parizek, B., Pollard, D., Price, S., Ren, D., Saito, F., Sato, T., Seddik, H., Seroussi, H., Takahashi, K., Walker, R., Wang, W.L., 2013a. Spatial sensitivities of the Greenland ice sheet to environmental changes (the SeaRISE project). Journal of Geophysical Research Earth Surface 1025–1044.
- Nowicki, S., Bindschadler, R., Abe-ouchi, A., Aschwanden, A., Choi, H., Fastook, J., Granzow, G., Gutowski, G., Herzfeld, U., Jackson, C., Johnson, J., Khroulev, C., Levermann, A., Lipscomb, W.H., Martin, M.A., Morlighem, M., Parizek, B., Pollard, D., Price, S., Ren, D., Saito, F., Sato, T., Seddik, H., Seroussi, H., Takahashi, K., Walker, R., Wang, W.L., 2013b. Spatial sensitivities of the antarctic ice sheet to environmental changes (the SeaRISE project). Journal of Geophysical Research Earth Surface 118, 1002–1024.
- Palm, S., Yang, Y., Herzfeld, U.C., 2019. ICESat-2 Algorithm Theoretical Basis Document for the Atmosphere, Part I: Level 2 and 3 Data Products, August 19, 2019. NASA ICESat-2 Project, 104pp.
- Petit, G., Luzum, B., 2010. Iers Conventions (2010) Iers Technical Note No. 36, International Earth Rotation and Reference Systems Service. Frankfurt, Germany.
- Shepherd, A., 2012. A reconciled estimate of ice-sheet mass balance. Science 338, 1183-1189. November.
- Shepherd, A., Ivins, E., Rignot, E., Smith, B., Van Den Broeke, M., Velicogna, I., Whitehouse, P., Briggs, K., Joughin, I., Krinner, G., et al., 2018. Mass balance of the Antarctic Ice Sheet from 1992 to 2017. Nature 558, 219–222.
- Smith, B., Hancock, D., Harbeck, K., Roberts, L., Neumann, T., Brunt, K., Fricker, H., Gardner, A., Siegfried, M., Adusumilli, S., Csatho, B., Holschuh, N., Nilsson, J., Paolo, F., 2019a. ICESat-2 Algorithm Theoretical Basis Document for Land Ice Along-Track Height Product, October 24, 2019. NASA ICESat-2 Project, 107pp.
- Smith, B., Fricker, H.A., Holschuh, N., Gardner, A.S., Adusumilli, S., Brunt, K.M., Csatho, B., Harbeck, K., Huth, A., Neumann, T., 2019b. Land ice height-retrieval algorithm for NASA's ICESat-2 photon-counting laser altimeter. Rem. Sens. Environ. 111352.
- Smith, B., Fricker, H., Gardner, A., Siegfried, M., Adusumilli, S., Csatho, B., Holschuh, N., Paolo, F., 2019c. ATLAS/ICESat-2 L3A Land Ice Height, Version 2 (Boulder, Colorado IISA)
- Stocker, T.F., Qin, H., Plattner, G.-K., Tignor, M., Allen, S.K., Boschung, J., Nauels, A., Xia, Y., Bex, V., Midgley, P.M. (Eds.), 2013. Climate Change 2013: the Physical Science Basis. Contribution of Working Group I to the Fifth Assessment Report of the Intergovernmental Panel on Climate Change. Cambridge University Press.
- Tedesco, M., Fettweis, X., Mote, T., Wahr, J., Alexander, P., Box, J., Wouters, B., 2013. Evidence and analysis of 2012 Greenland records from spaceborne observations, a regional climate model and reanalysis data. Cryosphere 7, 615–630.
- Trantow, T., Herzfeld, U.C., 2018. Crevasses as indicators of surge dynamics in the Bering-Bagley Glacier System, Alaska: numerical experiments and comparison to image data analysis. J. Geophys. Res.: Earth Surface 123 (8), 1615–1637.
- Van der Veen, C.J., 1998. Fracture mechanics approach to penetration of surface crevasses on glaciers. Cold Reg. Sci. Technol. 27 (1), 31–47.
- Wingham, D.J., Shepherd, A., Muir, A., Marshall, G.J., 2006. Mass balance of the antarctic ice sheet. Phil. Trans. Roy. Soc. Lond.: Mathematical, Physical and Engineering Sciences 364 (1844), 1627–1635.
- Yu, A.W., Harding, D.J., Dabney, P.W., 2016. Laser transmitter design and performance for the slope imaging multi-polarization photon-counting lidar (SIMPL) instrument. In: SPIE LASE. International Society for Optics and Photonics, 97260J–97260J.
- Zwally, H.J., Giovinetto, M., Li, J., Cornejo, H., Beckley, M., Brenner, A., Saba, J., Yi, D., 2005. Mass changes of the Greenland and Antarctic ice sheets and shelves and contributions to sea-level rise: 1992–2002. J. Glaciol. 51 (175), 509–527.